# Measurement of the Full Distribution of Persistent Current in Normal-Metal Rings

M. A. Castellanos-Beltran,[1,*] D. Q. Ngo,[1] W. E. Shanks,[1,†] A. B. Jayich,[1,‡] and J. G. E. Harris[1,2]

[1]*Department of Physics, Yale University, New Haven, Connecticut 06520, USA*
[2]*Department of Applied Physics, Yale University, New Haven, Connecticut 06520, USA*
(Received 12 November 2012; published 9 April 2013)

We have measured the persistent current in individual normal metal rings over a wide range of magnetic fields. From this data, we extract the first six cumulants of the single-ring persistent current distribution. Our results are consistent with the prediction that this distribution should be nearly Gaussian for diffusive metallic rings. This measurement highlights the sensitivity of persistent current to the mesoscopic fluctuations within a single isolated coherent volume.

PACS numbers: 73.23.Ra, 73.20.Fz

One of the fundamental archetypes in mesoscopic physics is a system whose volume is sufficiently small that electrons remain quantum coherent within it, yet sufficiently large and complex that its energy spectrum cannot, in practice, be calculated exactly. Such a coherent volume can be realized in a microfabricated metal device cooled to sufficiently low temperatures. The electronic spectrum of such a device will depend upon the angstrom-scale disorder within the metal, which is beyond the control of most fabrication techniques. As a result, the device's spectrum (and all related physical quantities) will be drawn randomly from an ensemble representing the possible realizations of the disorder within nominally identical (i.e., lithographically identical) devices.

The sample-to-sample fluctuations that result from this randomness are characterized by a distribution function $P_x$. Here, $x$ represents any physical quantity that depends upon the disorder, for example, the conductance $g$ or the persistent current $I$. These distributions play an important role in our understanding of how electrons flow through disordered materials, for example, in Anderson localization and the scaling theory of conductance [1–3]. For metallic samples (i.e., with mean conductance $\langle g \rangle \gg 1$ in units of $e^2/h$) calculations predict that $P_g$ and $P_I$ approach a Gaussian distribution as $\langle g \rangle \to \infty$ [4–9]. Deviations from Gaussianity at finite (but large) $\langle g \rangle$ reflect the approach of Anderson localization and the "breakdown" of single-parameter scaling that is due to a finite-sized system's vestigial sensitivity to the particular details of its microscopic disorder [3,4].

Several measurements of $P_g$ have been made in systems with $\langle g \rangle \lesssim 1$, including ballistic semiconductor quantum dots [10–12] and semiconductor wires near the localization threshold [13]. In this regime, experiments have found agreement with theory. However, in metallic samples, experiments to date have largely been confined to measurements of $\langle\langle g^2 \rangle\rangle$, the second cumulant of $P_g$. These measurements of $\langle\langle g^2 \rangle\rangle$ have found excellent agreement with theory in a broad range of circumstances [14–18]. However, little is known experimentally about mesoscopic

fluctuations (of $g$ or any other quantity) in metals beyond the second cumulant [18].

Measuring the full distribution of mesoscopic fluctuations in a metal device is challenging. In part this is because most experiments detect $g$, and so must attach leads to the device. These leads are much larger than the electrons' phase coherence length $L_\varphi$, and so contain a large number of coherent volumes that contribute in some degree [14,19,20] to the measured $g$. (The contribution from the leads is less important when $g \lesssim 1$, as in Refs. [10–13].) Since the fluctuations of each of these coherent volumes are assumed to be independent, higher cumulants of $P_g$ will tend to be suppressed in such a measurement, with the result that the observed fluctuations will appear more Gaussian than the actual $P_g$. The impact of the leads can be reduced by measuring $P_g$ in long wires (i.e., much longer than $L_\varphi$) but this ensures that the wire itself contains many coherent volumes, with the result that the observed fluctuations will again appear more Gaussian than $P_g$ [18].

However, it is possible to measure the mesoscopic fluctuations of *a single coherent volume* by detecting the persistent current $I$ in an isolated metal ring. This has been challenging in the past owing to the small signals involved [21], but it was recently shown that micromechanical torsional magnetometers can measure persistent current with very high sensitivity and low back-action [22,23]. This technique has been applied primarily to arrays of metal rings, with the result that the first two cumulants $\langle\langle I \rangle\rangle$ and $\langle\langle I^2 \rangle\rangle$ of $P_I$ were measured with high precision over a wide range of parameters [23,24]. However, the sensitivity achieved in Ref. [23] (as well as in other studies of individual metal rings [25,26]) did not allow for measurements of individual rings with adequate signal-to-noise ratio (SNR) to resolve the higher cumulants of $P_I$.

Here we describe measurements of the persistent current in a large number of individual rings. From these measurements we extract the first six cumulants of $P_I$, as well as other higher-order statistical properties of the persistent current. This is achieved by improving the SNR of the technique described in Refs. [22,23], and by combining

data from more than 400 effectively independent measurements. We find that our results agree with theoretical predictions to within the sensitivity of the measurements. Specifically, we find that the first six cumulants of $P_I$ are consistent with a Gaussian distribution. The small deviations from Gaussianity that are predicted by theory are too small to be detected in our experiment.

A typical device is shown in Fig. 1. It consists of a single-crystal Si cantilever supporting a single Al ring. The fabrication of these devices has been described previously [22,23]. The rings were fabricated via standard electron-beam lithography and were evaporated from a 99.999% purity Al source onto a Si substrate with a native oxide. In addition to the rings, Al wires and contact pads were co-deposited onto the same wafer to allow for transport characterization of the metal. Details of these transport measurements are given in the Supplemental Material [27]. These measurements show that $L_\varphi > 2\pi r$ ($r$ is the rings' mean radius) for the temperatures at which the persistent current is measured. They also provide the electrons' diffusion coefficient $D = 0.020 \pm 0.0015$ m$^2$/s.

The procedure for measuring the persistent current (PC) has also been described previously [23]. The cantilever's displacement is monitored by a laser interferometer. The signal from the interferometer is used to drive the cantilever in a phase-locked loop, allowing the cantilever's resonance frequency $\omega_m$ to be monitored. In the presence of an applied magnetic field $B$, the persistent current $I$ circulating in the ring produces a torque on the cantilever. This torque changes $\omega_m$, and $I$ is inferred from this change. Details are given in the Supplemental Material [23,27].

Measurements of the PC were made at temperatures 320 mK $< T <$ 365 mK, and magnetic fields 4 T $< B <$ 9 T (applied at an angle $\alpha = 45°$ relative to the rings' plane). This is well above the critical field of Al, ensuring that the rings are in their normal state. The large $B$ is

required to produce a detectable torque. It also simplifies the data analysis, as large $B$ within the metal of the ring strongly suppresses the effect of electron-electron interactions on the PC [24], allowing us to compare our results to independent-electron theory (though we note that for large $\langle g \rangle$ interactions are not predicted to make $P_I$ non-Gaussian [6–8]).

Measurements were made on eight different rings, with each ring on a separate cantilever. The full data sets from each ring, as well as the rings' dimensions and other properties, are shown in the Supplemental Material [27]. A typical measurement of $I(B)$ for one of these devices (ring #6) is shown in Fig. 2. The rapid oscillations in Figs. 2(a) and 2(b) are due to the Aharonov-Bohm (AB) effect: as $B$ is varied, the magnetic flux $\Phi = BA_\Phi \sin\alpha$ through the ring varies, causing $I(B)$ to oscillate with period $B_{\text{per}} = \Phi_0/(A_\Phi \sin\alpha)$. Here $A_\Phi = \pi r^2$ is the typical area enclosed by the electrons in the ring, and $\Phi_0 = h/e$. No higher harmonics of the AB oscillations were observed above the noise floor of the measurement.

The AB oscillations' amplitude (and upon closer inspection, their phase) varies on a field scale larger than $B_{\text{per}}$. These aperiodic modulations result from the fact that sweeping $B$ also varies the magnetic flux in the metal of the ring $\Phi_m \approx 2\pi r w B$, where $w$ is the ring's width. Because the ring represents a single coherent volume, its spectrum is expected to be randomized each time $\Phi_m$ changes by $\sim\Phi_0$ [28]. The ergodic hypothesis identifies this randomization with a new realization of the
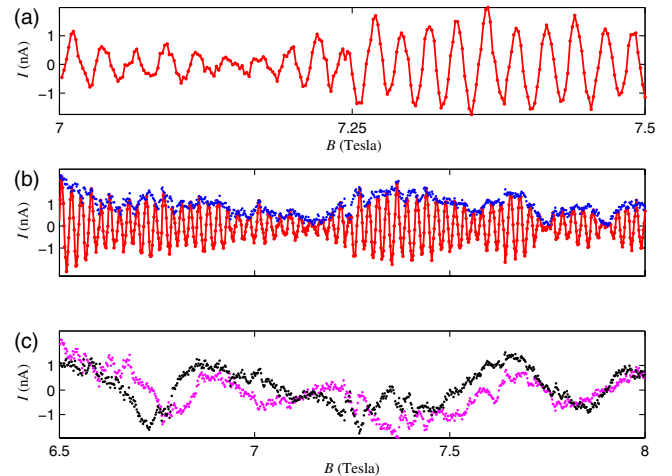


FIG. 2 (color online). Typical measurements of the persistent current in a single ring. (a) A small section of $I(B)$, the persistent current as a function the applied magnetic field. The oscillations are due to the Aharonov-Bohm effect, while the aperiodic modulation arises from flux inside the metal of the ring. (b) Red curve: $I(B)$ over a broader range of magnetic field. Blue curve: the envelope of $I(B)$. (c) The quadrature amplitudes $I^{(+)}$ (black) and $I^{(-)}$ (pink). The envelope in (b) and the quadratures in (c) were extracted by applying the Hilbert transform to the red trace in (b), as described in the Supplemental Material [27].
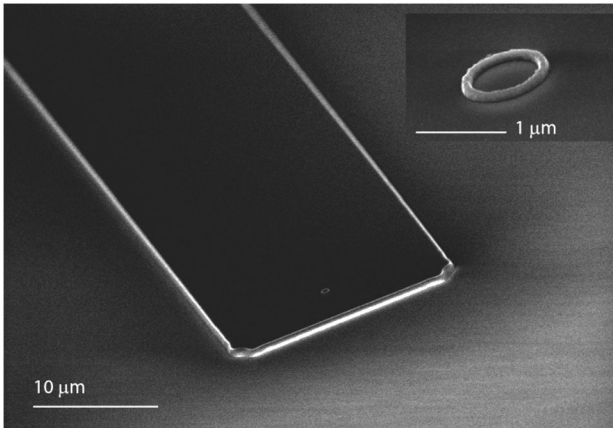


FIG. 1. Scanning electron micrograph of a cantilever with a single ring similar to the ones used in the experiment. Inset: magnified view of the ring. These images show the cantilever and ring prior to their release from the underlying SiO$_2$ layer.

microscopic disorder [28], so measurements of a single ring over a wide range of $B$ can be interpreted as measurements over a large number of lithographically identical rings. This allows us to use the eight physically distinct rings to measure a much larger number of effectively independent rings. As described below, the large number of effective samples is crucial for making an accurate estimate of the higher cumulants of $P_I$ [29].

Based on these considerations, at large magnetic fields the persistent current is expected to take the form [24]

$$I(\Phi_m, \Phi) = I^{(+)}(\Phi_m) \sin(2\pi\Phi/\Phi_0)$$
$$+ I^{(-)}(\Phi_m) \cos(2\pi\Phi/\Phi_0). \quad (1)$$

Theory makes three predictions concerning $I^{(+)}$ and $I^{(-)}$ (the quadrature amplitudes of the AB oscillations). The first is that they are stochastic functions of $\Phi_m$ characterized by a correlation function:

$$\langle I^{(+)}(\Phi_m)I^{(+)}(\Phi_m + \Delta\Phi_m)\rangle = \langle I^{(-)}(\Phi_m)I^{(-)}(\Phi_m + \Delta\Phi_m)\rangle$$
$$= \langle I^2 \rangle C(\Delta\Phi_m/\Phi_c) \quad (2)$$

that decays rapidly for $\Delta\Phi_m \gg \Phi_c$, where $\Phi_c$ is the correlation scale, which is typically a few times $\Phi_0$. Both $\Phi_c$ and the normalized correlation function $0 \leq C(x) \leq 1$ have been calculated in Ref. [24].

The second prediction is that the distribution of these quadrature amplitudes $P_{I^{(+)}} = P_{I^{(-)}} = P_I$ is Gaussian in the limit $\langle g \rangle \to \infty$ [6–9]. For finite but large $\langle g \rangle$ it is predicted [6,8,9] that the $n$th normalized cumulant (defined below) of the persistent current $\kappa_n \sim g^{2-n}$. In our samples $g \sim 10^4$, so these predicted deviations from Gaussianity are well below our present sensitivity (and we note that some $\kappa_n$ are suppressed still further by a large magnetic field [9]).

Last, correlations between $I^{(+)}$ and $I^{(-)}$ are predicted to be absent [24].

To test these three predictions, we first use the $I(B)$ data from one sample (ring #6, see Supplemental Material [27] for the full data sets and ring parameters) to determine the normalized autocorrelation of the persistent current, $\langle I(B)I(B + \Delta B)\rangle/\langle I^2 \rangle$. The result is plotted in Fig. 3, and shows AB oscillations whose envelope initially decays on a field scale that is a few times $\Phi_0/2\pi rw$, in qualitative agreement with the discussion above. After this initial decay the envelope does not approach zero, but instead undergoes apparently random fluctuations. These fluctuations are due to the finite size of the data set, and are discussed below.

We can make a more quantitative comparison with theory by fitting the autocorrelation data in Fig. 3 to the prediction [24] that it should consist of AB oscillations whose envelope is given by $C(\Delta B/B_c)$, where $B_c = \Phi_c/2\pi rw$. The resulting fit is shown as the red line in Fig. 3. The fit parameters are $B_c^{(6)} = 37$ mT and $B_{per}^{(6)} = 25$ mT (where the superscript denotes the ring no.), in good agreement with the dimensions of the ring. The
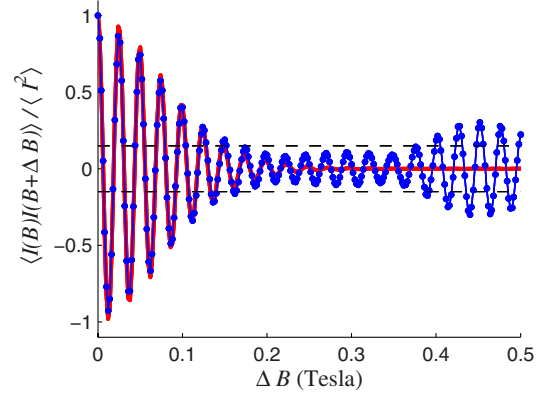


FIG. 3 (color online).   Autocorrelation of the persistent current in a single ring. The blue curve is the normalized autocorrelation of the $I(B)$ data from ring #6, while the red curve is a fit to theory. Only data with $\Delta B < 0.3$ was used for the fit. The expected error in the autocorrelation (due to the finite size of the data set) is indicated by the dashed horizontal lines. Similar behavior was observed in all eight rings.

autocorrelation data from the other seven rings showed comparable agreement with the theoretical prediction, although the fitted values of $B_c$ varied from ring to ring (all values of the $B_c^{(i)}$ are given in the Supplemental Material [27]). This analysis provides us with two useful results. The first result is the agreement between the measured and predicted form of $C(x)$, which justifies our use of the analytic expression [24] for $C(x)$ in the analyses below. The second result is the determination of the correlation field $B_c^{(i)}$ for each ring, which will also be used below.

To determine the form of the distribution $P_I$ from our measurements, we begin by applying the Hilbert transform to the $I(B)$ data from each ring. This provides the quadrature amplitudes $I^{(+)}(B)$ and $I^{(-)}(B)$, as shown in Fig. 2(c). It is then straightforward to compute the cumulants of $I^{(+)}$ and $I^{(-)}$, e.g., from their moments. Since there is no physical distinction between $I^{(+)}$ and $I^{(-)}$ when $\Phi_m \gg \Phi_0$, we consider the average of their cumulants: $\langle\langle I^n \rangle\rangle \equiv \frac{1}{2}(\langle\langle (I^{(+)})^n \rangle\rangle + \langle\langle (I^{(-)})^n \rangle\rangle)$. To account for variations between the rings (e.g., of $D$, $r$, and $T$), the contribution to $\langle\langle I^n \rangle\rangle$ from each ring is normalized by the variance $\langle\langle I^2 \rangle\rangle$ of that ring, giving the normalized cumulant $\kappa_n \equiv \langle\langle I^n \rangle\rangle/\langle\langle I^2 \rangle\rangle^{n/2}$ for the entire data set.

The first several $\kappa_n$ are plotted as blue circles in Fig. 4(a). The prediction that $P_I$ is Gaussian (corresponding to $\kappa_n = 0$ for all $n \geq 3$) is indicated by the black circles in Fig. 4(a). The data appear qualitatively consistent with a Gaussian distribution; however, to make a meaningful comparison between experiment and theory we estimate the uncertainty in these values. The two most important sources of uncertainty in the measurements of $\kappa_n$ are the finite SNR of the $I(B)$ data and the finite size of the data set from which the $\kappa_n$ are calculated. We estimate the impact of the former by applying standard error-propagation
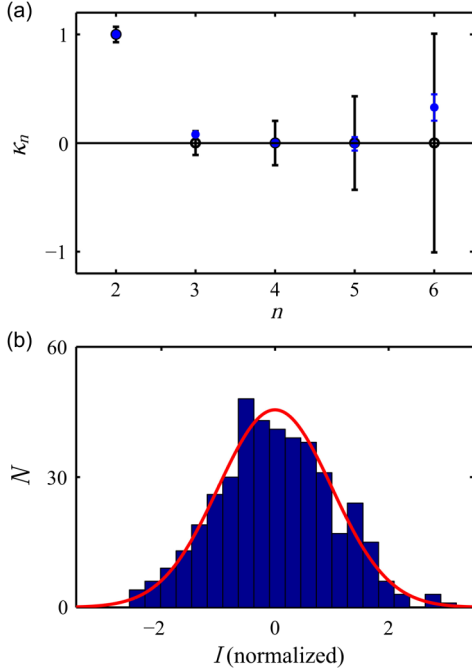
FIG. 4 (color online). The measured distribution of persistent current. (a) Cumulants of the persistent current distribution, calculated from the combined data for all eight rings. Blue circles are the measured cumulants, and black circles are the cumulants expected for a Gaussian distribution. Black error bars: statistical uncertainty from the finite sample size. Blue error bars: statistical uncertainty from the finite signal-to-noise ratio. (b) Histogram of the observed persistent currents. To reduce oversampling artifacts, the data is first binned to give data points that are approximately independent. The solid line is the no-free-parameters prediction.

techniques to the known uncertainty in each $I(B)$ measurement. This procedure is described in the Supplemental Material [27], and leads to the blue error bars in Fig. 4(a).

The finite size of the data set leads to a statistical uncertainty $\delta\kappa_n$ in the estimate of each $\kappa_n$. If the data sets for $I^{(+)}(B)$ and $I^{(-)}(B)$ each consisted of uncorrelated data points, then values for the $\delta\kappa_n$ could be found in standard statistics references. However, it is clear from Figs. 2(c) and 3 that each quadrature of the AB oscillations contains correlations that are characterized by the function $C(\Delta B/B_c)$. In this case the $\delta\kappa_n$ depend upon the form of $C(x)$, the value of $B_c$, and the value of $B_{\text{span}}$, the range of $B$ over which the PC is measured [29],

$$\delta\kappa_n \equiv \langle\kappa_n^2\rangle^{1/2} = \left(n!c_n \frac{B_c}{B_{\text{span}}}\langle\kappa_2\rangle^n\right)^{1/2},$$

$$c_n = \int_{-\infty}^{\infty}(C(x))^n dx \tag{3}$$

(where the dependence of $B_c$, $B_{\text{span}}$, and $c_n$ upon the ring no. has been suppressed). The black error bars in Fig. 4(a) correspond to the $\delta\kappa_n$ calculated from Eq. (3). Since $\delta\kappa_n < 1$ only for $n < 7$, we plot the results only up to $\kappa_6$.

In addition to calculating the cumulants of $P_I$ from our data, we can also plot the measured $P_I$ in the form of a histogram of the $I^{(+)}(B)$ and $I^{(-)}(B)$ data. To reduce oversampling artifacts in this histogram, we first bin the $I^{(+)}(B)$ and $I^{(-)}(B)$ data into a smaller data set. We choose the size of this smaller data set to correspond to the number of effectively independent data points in the entire data set [29] (i.e., from all eight physically distinct rings): $N_{\text{eff}} = 2\sum_{i=1}^{8} B_{\text{span}}^{(i)}/c_n^{(i)} B_c^{(i)} \approx 412$ (the factor of 2 in this expression arises from the two quadratures). Here we have used $n = 2$ somewhat arbitrarily, but we note that $N_{\text{eff}}$ depends only weakly upon the choice of $n$. As in the calculations of the $\kappa_n$, the $I^{(+)}(B)$ and $I^{(-)}(B)$ data from each different ring are normalized by their own variance to account for differences among the rings. The histogram of the resulting data set is shown in Fig. 4(b), along with the no-free-parameter prediction that this histogram should be Gaussian with zero mean and unit variance.

We can use these results to understand the apparently random fluctuations of the autocorrelation data in Fig. 3. At large $\Delta B$, the data are expected to be uncorrelated [i.e., $C(x)$ approaches zero for large $x$]. However, the standard error of the autocorrelation of a data set consisting of $N$ independent samples is [30] $\delta C = 1/\sqrt{N}$. The data set for ring #6 contains $N_{\text{eff}}^{(6)} = 44$ independent samples; thus at large $\Delta B$ the envelope of the autocorrelation in Fig. 3 should have a typical value $\approx 0.15$. This value is indicated by the dashed lines in Fig. 3, and is in agreement with the data.

Last, we test our data for correlations between the quadrature amplitudes. From the $I^{(+)}(B)$ and $I^{(-)}(B)$ data it is straightforward to calculate the experimental value of $\rho_{+-} \equiv \text{cov}(I^{(+)}, I^{(-)})/\sqrt{\langle\langle I^{(+)2}\rangle\rangle\langle\langle I^{(-)2}\rangle\rangle}$ which is predicted [24] to be zero. From our data we find $\rho_{+-} = 0.02 \pm 0.05$, where the uncertainty arises from the finite size of the data set. This result is consistent with the prediction that $I^{(+)}(B)$ and $I^{(-)}(B)$ should be independent of each other.

*Present address: National Institute for Standards and Technology, Boulder, CO 80305, USA.
†Present address: Department of Electrical Engineering, Princeton University, Princeton, NJ 08544, USA.
‡Present address: Department of Physics, UCSB, Santa Barbara, CA 93106, USA.

[1] P. W. Anderson, Phys. Rev. **109**, 1492 (1958).
[2] E. Abrahams, P. W. Anderson, D. C. Licciardello, and T. V. Ramakrishnan, Phys. Rev. Lett. **42**, 673 (1979).
[3] B. Shapiro, Philos. Mag. B **56**, 1031 (1987).
[4] B. L. Al'tshuler, V. E. Kravtsov, and I. V. Lerner, Sov. Phys. JETP **64**, 1352 (1986).
[5] M. C. W. van Rossum, I. V. Lerner, B. L. Altshuler, and T. M. Nieuwenhuizen, Phys. Rev. B **55**, 4710 (1997).
[6] R. A. Smith and V. Ambegaokar, Europhys. Lett. **20**, 161 (1992).
[7] H. J. Bussemaker and T. R. Kirkpatrick, Phys. Rev. B **56**, 4529 (1997).
[8] M. Houzet, Phys. Rev. B **82**, 161417 (2010).
[9] J. Danon and P. W. Brouwer, Phys. Rev. Lett. **105**, 136803 (2010).
[10] A. M. Chang, H. U. Baranger, L. N. Pfeiffer, K. W. West, and T. Y. Chang, Phys. Rev. Lett. **76**, 1695 (1996).
[11] J. A. Folk, S. R. Patel, S. F. Godijn, A. G. Huibers, S. M. Cronenwett, C. M. Marcus, K. Campman, and A. C. Gossard, Phys. Rev. Lett. **76**, 1699 (1996).
[12] A. G. Huibers, S. R. Patel, C. M. Marcus, P. W. Brouwer, C. I. Duruöz, and J. S. Harris, Jr., Phys. Rev. Lett. **81**, 1917 (1998).
[13] W. Poirier, D. Mailly, and M. Sanquer, Phys. Rev. B **59**, 10856 (1999).
[14] R. A. Webb *et al.*, in *Physics and Technology of Submicron Structures*, edited by H. Heinrich, G. Bauer, and F. Kuchar (Springer-Verlag, Berlin, 1988), p. 98.
[15] A. Benoit *et al.*, in *Anderson Localization*, edited by T. Ando and H. Fukuyama (Springer-Verlag, Berlin, 1988), p. 346.
[16] C. W. J. Beenakker and H. van Houten, Solid State Phys. **44**, 1 (1991).
[17] S. Washburn and R. A. Webb, Rep. Prog. Phys. **55**, 1311 (1992).
[18] V. Fal'ko, I. Lerner, O. Tsyplyatyev, and I. Aleiner, Phys. Rev. Lett. **93**, 159701 (2004).
[19] V. Chandrasekhar, D. E. Prober, and P. Santhanam, Phys. Rev. Lett. **61**, 2253 (1988).
[20] H. U. Baranger, A. D. Stone, and D. P. DiVincenzo, Phys. Rev. B **37**, 6521 (1988).
[21] L. Saminadayar, C. Bauerle, and D. Mailly, Encycl. Nanosci. Nanotech. **3**, 267 (2004).
[22] A. C. Bleszynski-Jayich, W. E. Shanks, B. R. Ilic, and J. G. E. Harris, J. Vac. Sci. Technol. B **26**, 1412 (2008).
[23] A. C. Bleszynski-Jayich, W. E. Shanks, B. Peaudecerf, E. Ginossar, F. von Oppen, L. Glazman, and J. G. E. Harris, Science **326**, 272 (2009).
[24] E. Ginossar, L. I. Glazman, T. Ojanen, F. von Oppen, W. E. Shanks, A. C. Bleszynski-Jayich, and J. G. E. Harris, Phys. Rev. B **81**, 155448 (2010).
[25] V. Chandrasekhar, R. A. Webb, M. J. Brady, M. B. Ketchen, W. J. Gallagher, and A. Kleinsasser, Phys. Rev. Lett. **67**, 3578 (1991).
[26] H. Bluhm, N. C. Koshnick, J. A. Bert, M. E. Huber, and M. A. Moler, Phys. Rev. Lett. **102**, 136802 (2009).
[27] See Supplemental Material at http://link.aps.org/supplemental/10.1103/PhysRevLett.110.156801 for information on the transport characterization of the deposited metal, the data analysis used for the measurement of the persistent current, the parameters of the individual rings, and the complete data set from each ring.
[28] P. A. Lee and A. D. Stone, Phys. Rev. Lett. **55**, 1622 (1985).
[29] O. Tsyplyatyev, I. L. Aleiner, V. I. Falko, and I. V. Lerner, Phys. Rev. B **68**, 121301(R) (2003).
[30] M. G. Kendall and A. Stuart, *The Advanced Theory of Statistics* (Griffin, London 1976), Vol. 1, 4th ed.

# Measurement of the full distribution of the persistent current in normal-metal rings: Supplementary Information.

M. A. Castellanos-Beltran,[1][*] D. Q. Ngo,[1] W. E. Shanks,[1] A. B. Jayich,[1] and J. G. E. Harris[1,2]

[1]Department of Physics, Yale University, New Haven, CT, 06520, USA

[2]Department of Applied Physics, Yale University, New Haven, CT, 06520, USA

## 1    Transport measurements

The main paper compares our measurements of the persistent current in normal metal rings to predictions of a theoretical model based on diffusive, non-interacting electrons (3). This theory depends explicitly upon two parameters of the rings: their diffusion coefficient $D$ and their spin-orbit scattering length $L_{SO}$. This theory also implictly assumes that the rings' phase coherence length ($L_\phi$) is much greater than the rings' circumference $L$. The persistent current data presented in the main paper can be compared with this theory by taking $D$ and $L_{SO}$ as fitting parameters (and assuming $L_\phi \gg L$), but in order to constrain this comparison more tightly, we have used transport measurements to directly measure $D$, $L_{SO}$, and $L_\phi$. Transport measurements similar to those described in Ref. (2) were performed on an aluminum wire codeposited with the rings studied in this article. The wire was deposited on the same wafer as the rings. It had a length $L = 255\,\mu$m, a width $w = 105$ nm (determined from SEM images) and a thickness $t = 115$ nm (determined from AFM measurements).

Measurements of the wire's resistance were performed using a bridge circuit similar to that of Ref. (6): a three terminal arrangement was used here as one of the four original leads was unintentionally blown out as the sample cooled to 4.2 K. One side of the sample was connected to the bridge and the voltage probe through separate leads, while the other side of the sample was connected to ground and the bridge through the same lead. The sample resistance was distinguished from the lead resistance by measuring the resistance of the sample as it transitioned from the superconducting to the normal state as the magnetic field was swept at a temperature below the wire's transition temperature $T_c$. A measurement of this transition is shown in Fig. 1a.

The diffusion constant $D$ was then calculated using the Einstein relation ($\rho^{-1} = e^2 g D$), with $e$ being the electron charge and $g$ the electron density of states per unit volume at the Fermi level for aluminum (7). The resistance was measured to be 288 $\Omega$. Based on the film dimensions, we infer a resistivity $\rho = 1.36 \times 10^{-8} \pm 0.1\,\Omega$m. This corresponds to a diffusion constant $D_\rho = 0.02 \pm 0.0015\,\mathrm{m^2/s}$. We label $D_\rho$ the diffusion constant extracted from this measurement of $\rho$.

We also performed magnetoresistance measurements on the same wire at temperatures above $T_c$ in order to extract $L_\phi$ and $L_{SO}$. The magnetoresistance in the aluminum wire

---

[*]To whom correspondence should be addressed; E-mail: manuel.castellanosbeltran@yale.edu.

has contributions from weak localization as well as Maki-Thompson superconducting fluctuations. The analytical form for the weak-localization correction to the resistance of a 1-D wire in a magnetic field is given by

$$\frac{dR^{WL}}{R} = \frac{R(B) - R(B=0)}{R(B=0)} = \frac{3}{2}f_1\left(B, b(L_2)\right) - \frac{1}{2}f_1\left(B, b(L_\phi)\right) \tag{1}$$

where $1/L_2^2 = 1/L_\phi^2 + 4/3L_{SO}^2$, $L_\phi$ is the electron phase coherence and $L_{SO}$ is the spin-orbit coupling length. The functions $f_1(B, B1)$ and $b(l)$ are defined in Ref. (2). The Maki-Thompson contibrution is given by

$$\frac{dR^{MT}}{R} = -\beta\left(\frac{T}{T_c}\right)f_1\left(B, b(L_\phi)\right) \tag{2}$$

where $\beta(t)$ is a function that diverges logarithmically when $t \to 1$ (see Ref. (2) and references therein). Equation 2 is only valid provided

$$B \ll \frac{k_B T}{4De}\ln\left(T/T_c\right). \tag{3}$$

Fits were done using the sum of both equations 1 and 2:

$$\frac{dR}{R} = \frac{dR^{WL}}{R} + \frac{dR^{MT}}{R} \tag{4}$$

Magnetoresistance measurements were made at a series of temperatures above $T_c$ between 1.8 and 12 K. $L_{SO}$ was obtained from fits of the magnetoresistance to Eq. 4 measured at the highest temperatures ($T = 9 - 12$ K), where $L_{SO}$ was measured to be $1.54 \pm 0.06\,\mu\text{m}$.[1] For fits of the lower temperature data, $L_{SO}$ was fixed at this value, so $L_\phi$ was the only fitting parameter. Fits to the magnetoresistace data using Eq. 4 are shown in Fig. 1b. The constraint set by Eq. 3 upon the validity of Eq. 2 sets the limit over which the fits were performed.

The temperature dependence of $L_\phi$ can be explained based on the different contributions to the inelastic collisions of the electrons. Theory predicts that $\tau_\phi$ is limited by inelastic collisions with other electrons through the screened Coulomb interactions ($\tau_{ee}$), with phonons ($\tau_{ep}$) and with extrinsic sources such as magnetic impurites. The latter should be negligible for the high purity aluminum source used and since no magnetic impurity has been observed to behave as a localized moment when dissolved in aluminum (7). The fitted values of $L_\phi$ as a function of temperature are shown in Fig. 1c. The function used to fit to the data is $L_\phi = \sqrt{D\tau_\phi}$, where

$$\tau_\phi^{-1} = A_{ep}T^3 + A_{ee}T^{2/3}. \tag{5}$$

$A_{ep}$ and $A_{ee}$ are fit parameters. The first term of Eq. 5 corresponds to the electron-phonon scattering rate, $\tau_{ep}^{-1} = A_{ep}T^3$. From our fit we find that $A_{ep} = 2.0 \pm 0.2 \times 10^7\text{s}^{-1}\text{K}^{-3}$ which is within a factor of two of previoulsy measured electron-phonon coefficients for comparable Aluminum wires (2, 8).

The second term of Eq. 5 corresponds to electron-electron scattering. The wire (and rings) studied here had a width and thickness smaller than $L_\phi$. Therefore, the quasi-1D

---

[1]The error bar in $L_{SO}$ was obtained from the following analysis: each of the fits to the four traces at the tempratures $T = 9$, 10, 11 and 12 K provided the same $L_{SO}$ within the fit error. The errorbars from the obtained values of $L_{SO}$ at each temperature are based on the goodness of the fits. Then we do a weighted average of the obtained values of $L_{SO}$ and the error is correspondingly $\sigma = 1/\sqrt{\Sigma_{i=1}^4 1/\sigma_{i,fit}^2}$ .
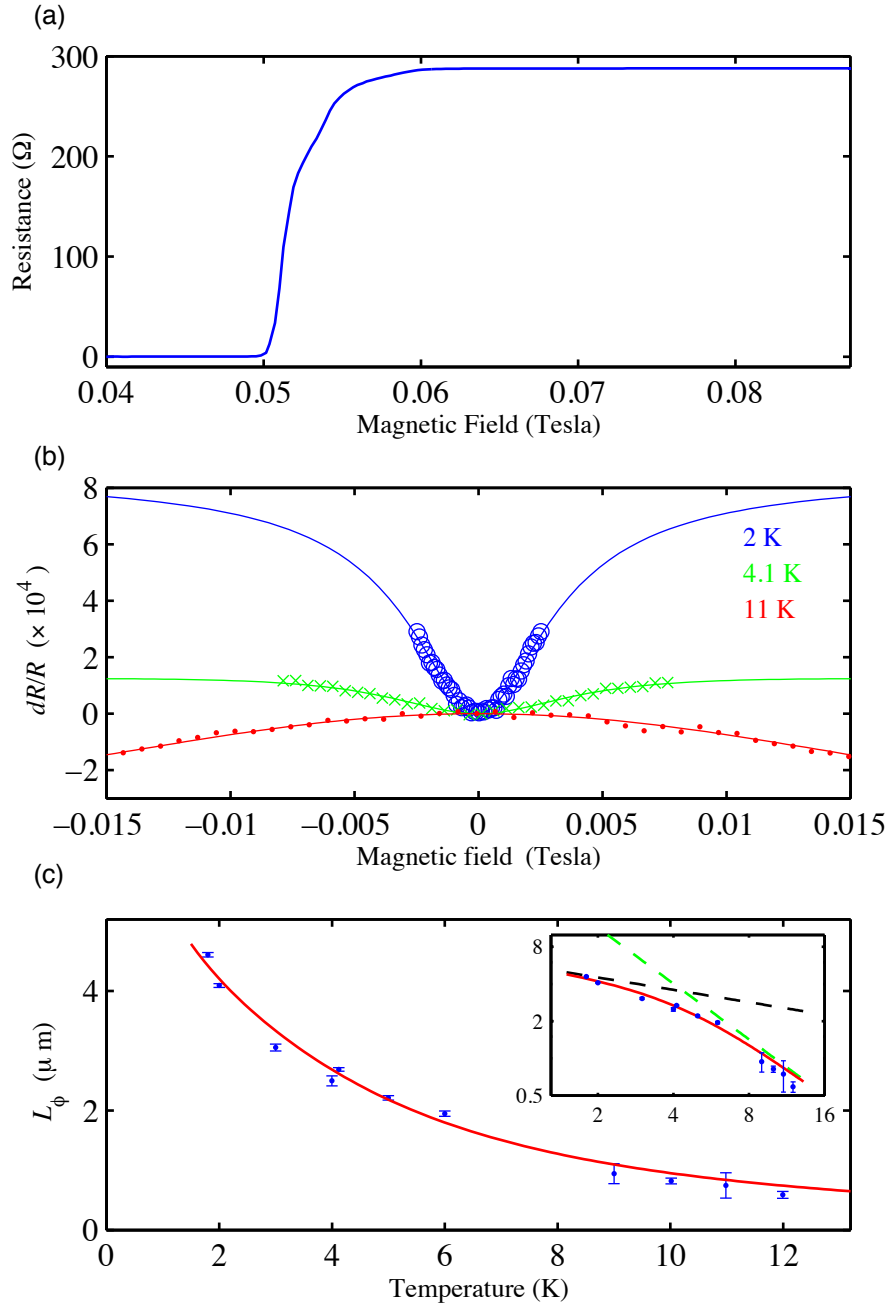
Figure 1: (a) Resistance measurement of the aluminum wire as the magnetic field is swept through the critical field $B_c$ at a temperature $T = 300\,\text{mK}$. The measured resistance in the normal state was 288 $\Omega$. Due to the loss of one the leads, in series with the sample, we measured a lead resistance of 22 $\Omega$. This finite resistance is observed even when at $|B| < B_c$ and $T < T_c$, and it has been subtracted from the trace. (b) Magnetoresistance data for $T = 2\,\text{K}$ ($\circ$), $4.1\,\text{K}$ ($\times$) and $11\,\text{K}$ (.) and fits (solid lines). The trace for 11 K has been multiplied by 20. At low temperatures, superconducting fluctuations are the dominant effect observed in the magnetoresistance measurements. The weak localization becomes the dominant effect at $T > 8\,\text{K}$. (c) Phase coherence length $L_\phi$ extracted from fitting the magnetoresistance data as a function of temperature (points) and fit (solid line) to the expected coherence length assuming both electron-electron and electron-phonon contributions. Inset: Log plot showing $\tau_{e-p}$ and $\tau_{ee}$ contribution as dashed-green and dashed-black lines respectively.

3

prediction for electron-electron interaction applies and the expression for $\tau_{ee}$ according to Ref. (9) is

$$\tau_{ee}^{-1} = A_{ee}T^{2/3} = \left[\frac{R_\square e^2 k_B \sqrt{D}}{2\sqrt{2}\hbar^2 w}\right]^{2/3} T^{2/3}. \tag{6}$$

The fitted valued for $A_{ee}$ is $0.65 \pm 0.03 \times 10^9 \text{s}^{-1}\text{K}^{-2/3}$. The expected theoretical value based on Eq. 6 and a diffusion constant of $D = 0.020\,\text{m}^2/\text{s}$ is $A_{ee} = 0.15 \times 10^9 \text{s}^{-1}\text{K}^{-2/3}$. Although there is a large discrepancy betwen the expected and fitted value of $A_{ee}$, the primary purpose of these transport measurements is to show that $L_\phi$ is greater than the circumference of the rings $L = 1.8$ and $2.8$ $\mu$m; therefore we did not look further into this disagreement.[2]

The value for the diffusion constant extracted from the resistivity measurement can then be compared with the diffusion constant extracted from the persistent current measurement (Fig. 2). Using a similar analysis to that explained in Ref. (3) we extract a value of $D_{PC} = 0.021 \pm 0.002\,\text{m}^2/\text{s}$. We label this value as $D_{PC}$ to distinguish from $D_\rho$. $D_{PC}$ and $D_\rho$ differ by about 5%. This seems reasonable given differences between wire cross section and ring cross section plus statistical uncertainty in $D_{PC}$.

## 2    Data Analysis

We inferred the persistent current in each ring by measuring the resonance frequency of the cantilever into which the ring was integrated by driving the cantilever in a phase-locked loop (10). The method used to infer the current is explained in the supplementary information of Ref. (2). Here we briefly review this analysis.

As it was shown in Ref. (3), the presence of magnetic field $B_m$ inside the metal of the ring leads to an aperiodic modulation of the persistent current oscillations and a change in the flux dependence of of the persistent current from the simpler case where there is only a pure Aharonov-Bohm flux $\phi$ threading the ring. This change is the modification of the time-reversal relation from $I(\phi) = -I(-\phi)$ to $I(B_m, \phi) = -I(-B_m, -\phi)$ . As a result, the current is no longer odd in the Aharonov-Bohm flux $\phi$ and it takes the more general form at fixed $B_m$

$$I(\phi) = \sum_p I_{h/pe}^+ \sin(2\pi p\frac{\phi}{\Phi_0}) + I_{h/pe}^- \cos(2\pi p\frac{\phi}{\Phi_0}) \tag{7}$$

where the variables $I_{h/pe}^+$ and $I_{h/pe}^-$ are stochastic variables that vary with the magnetic field $B_m$ as well as with microscopic disorder, and $\Phi_0 = h/e$ is a flux quantum. Determining the distribution of $I_{h/pe}^+$ and $I_{h/pe}^-$ is the central point of the main paper.

We monitor the the cantilever frequency as we vary the magnetic field. The cantilever's deflection leads to a rotation of the sample, responsible for the coupling between the persistent current and the cantilever. When $\theta \neq \pi/2$ (where $\theta$ is the angle between the plane of the ring and the applied magnetic field $B$), the frequency change is dominated by the following term:

$$
\begin{aligned}
\delta f \quad = \quad & -\frac{ABf_0\gamma_m}{kLx_{\text{tip}}} \cos(\theta) \sum_p J_1\left(2\pi p\frac{AB\cos(\theta)}{\Phi_0}\frac{\gamma_m x_{\text{tip}}}{L}\right) \times \\
& \left(I_{h/pe}^+ \cos(2\pi p\frac{BA\sin\theta}{\Phi_0}) - I_{h/pe}^- \sin(2\pi p\frac{BA\sin\theta}{\Phi_0})\right)
\end{aligned}
\tag{8}
$$

---

[2]In addition, it has been pointed out that close to the superconducting transition, the electron-electron inelastic scattering rate can be modified due to superconducting fluctuations (8). These fluctuations may alter the numerical coefficient $A_{ee}$.
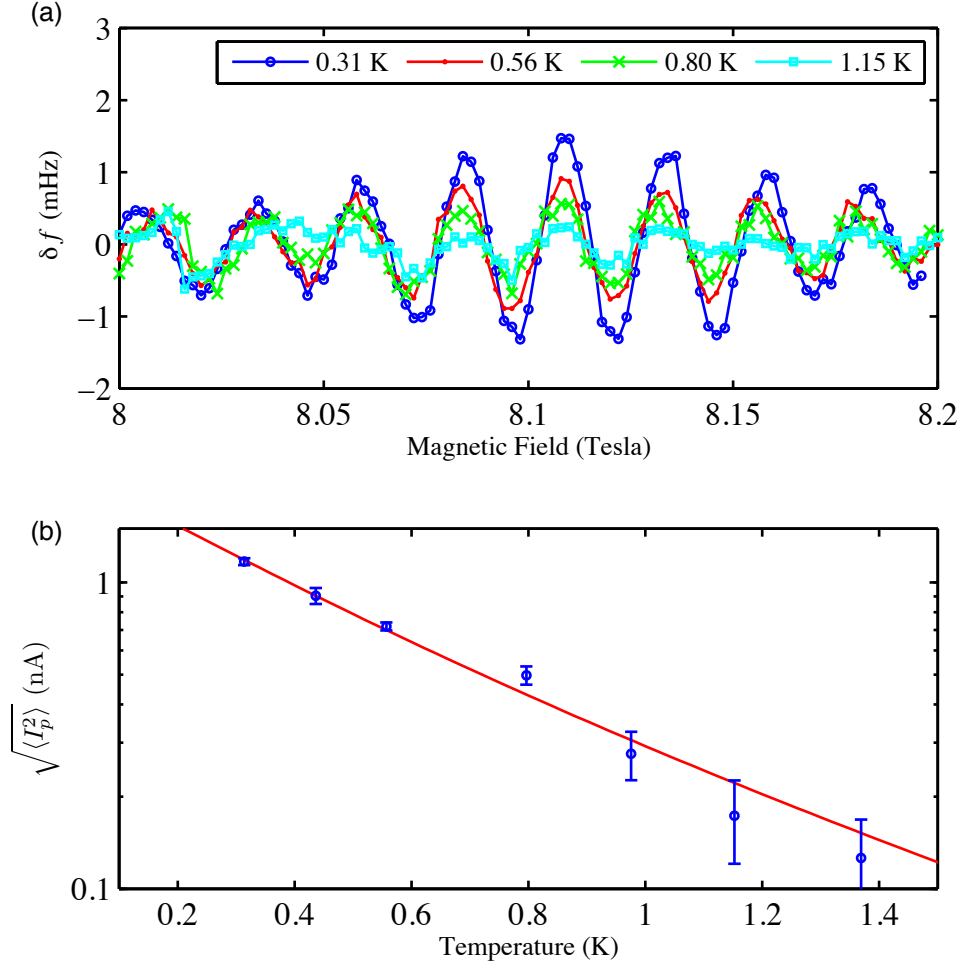
4

Figure 2: (a) Frequency shift versus magnetic field for a ring of radius $r = 296$ nm at different temperatures. The amplitude of frequency oscillations decreases with increasing temperature as expected. The amplitude of the frequency oscillations is converterted into current oscillations amplitude and plotted as a function of temperature in (b). Data (circles) and a fit (solid line) based on analysis similar to that explained in Ref. (3) are plotted. From the fit we estimate a diffusion constant of $D = 0.021 \pm 0.02$.

where $A$ is the area of the ring, $f_0$ is the natural resonance frequency of the cantilever, $\gamma_m$ is the ratio between the slope of the cantilever and the factor $x_{\text{tip}}/L$ for the flexural mode $m$. For $m = \{1, 2\}$, $\gamma_m = \{1.377, 4.788\}$. $k$ is the cantilever spring constant, $L$ is the length of the cantilever, $x_{\text{tip}}$ is the amplitude of oscillation at the tip of the cantilever, and $J_1(x)$ is the first Bessel function of the first kind.

At the temperatures of our experiment the current is dominated by the first harmonic, $p = 1$. Thus, for the analysis of the data shown in the main paper we use what in the supplementary online information (SOI) of Ref. (2) is refered to as method B: we assume that the signal only has the $p = 1$ component in Eq. 8 and that the argument of the Bessel function varies only weakly over a given data set. In that case, the change in frequency is essentially the derivative of the persistent current (again ignoring all terms for $p > 1$).

$$\frac{\partial I}{\partial B} \approx -\delta f \frac{2\pi A \sin\theta}{\Phi_0} \left[ \frac{AB\nu\gamma_m}{kLx_{\text{tip}}} \cos(\theta) J_1 \left( 2\pi p \frac{AB \cos(\theta)}{\Phi_0} \frac{\gamma_m x_{\text{tip}}}{L} \right) \right]^{-1}$$

In order to estimate the current this quantity can be numerically integrated. However, since we are interested in the statisitics of the variables $I_{h/e}^{\pm}$, we perform the analysis on $I'$ defined as

$$I'(B) = \frac{\Phi_0}{2\pi A \sin\theta} \frac{\partial I}{\partial B} \tag{9}$$

The normalization is such that the oscillations of $I'(B)$ have the same amplitude as those in $I(B)$. The reason we use $I'$ is that the numerical integration can introduce unwanted correlations in the values of the variables $I_{h/e}^{\pm}$.

## 2.1 Drift removal

We measured cantilevers similar to the ones shown in Fig. 3. We fabricated long ($l \sim 400\mu$m) and short ($l \sim 100\,\mu$m) cantilevers, with three different widths ($w = 20, 40$ and $60\ \mu$m). The signal $\delta f$ was larger for the shortest cantilevers. However, their noise peformance was very poor, presenting frequency noise with a power dependence $\sim 1/f^n$ with $n \approx 2$, preventing our measurements from achieving the thermal noise limit. However, for the long cantilevers the noise performance of the frequency measurement did reach the thermal noise limit (see Sect. 2.2.1).
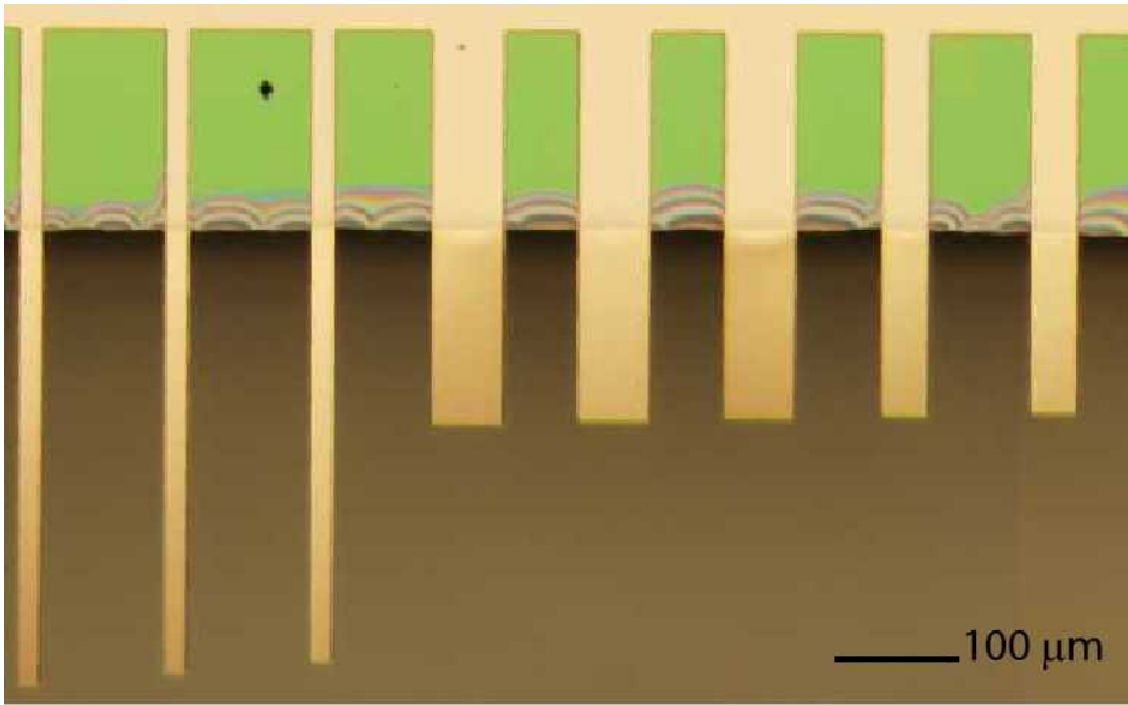
Figure 3: Optical micrograph of cantilevers similar to those used for the measurement of persistent current in the main text. The ring sample on each cantilever is not visible.

Raw data of the frequency measurements of two kind of cantilevers are shown in figures 4 and 5. In both figures we can see a drift in the cantilever's resonance frequency with time, but with very different characterisitics. In Fig. 4 the Aharonov-Bohm (AB) oscillations can be easily distinguished on top of a mostly magnetic-field dependent drift. This drift is removed using MATLAB's local regression algorithm for the LOWESS (Locally Weighted Scatterplot Smoothing) routine with a first degree polynomial. We have observed that if we choose the window of the LOWESS routine to be the equivalent of 5 AB oscillations, the peak of our signal in its Fourier transform is unchanged by the drift removal process.

For a thermally limited frequency measurement, shorter cantilevers should have a greater signal-to-noise ratio, but we found that, in practice, their frequency noise was significantly worse than the longer cantilevers. Thus, for shorter cantilevers, the frequency measurements were not thermally limited. This is obvious in figures 5a and b where it is not possible to discern the AB oscillations at first sight. In Fig. 5c and d we show the averaged data and their spectral densities with and without LOWESS drift removal in order to show that our procedure does not convert a noise shoulder into a peak.
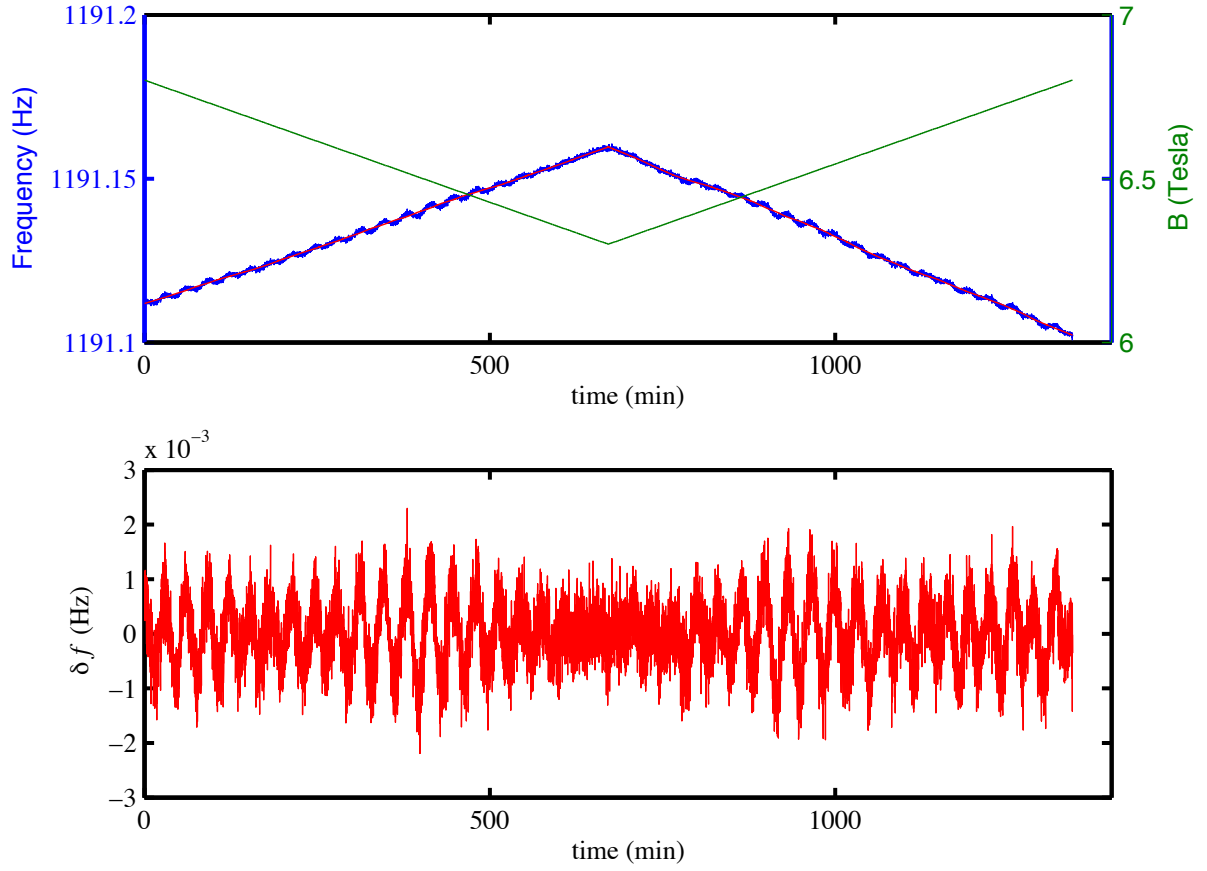
Figure 4: (a) Cantilever frequency (blue left axis) as a function of time as the magnetic field (green right axis) is varied for sample 6. On top of a magnetic-field-dependent background, the oscillations due to the persistent current are obvious and the drift in the cantilever frequency is easily removed by using local regression. After substracting the drift calculated using LOWESS (red trace) we obtain the oscillations shown in (b).
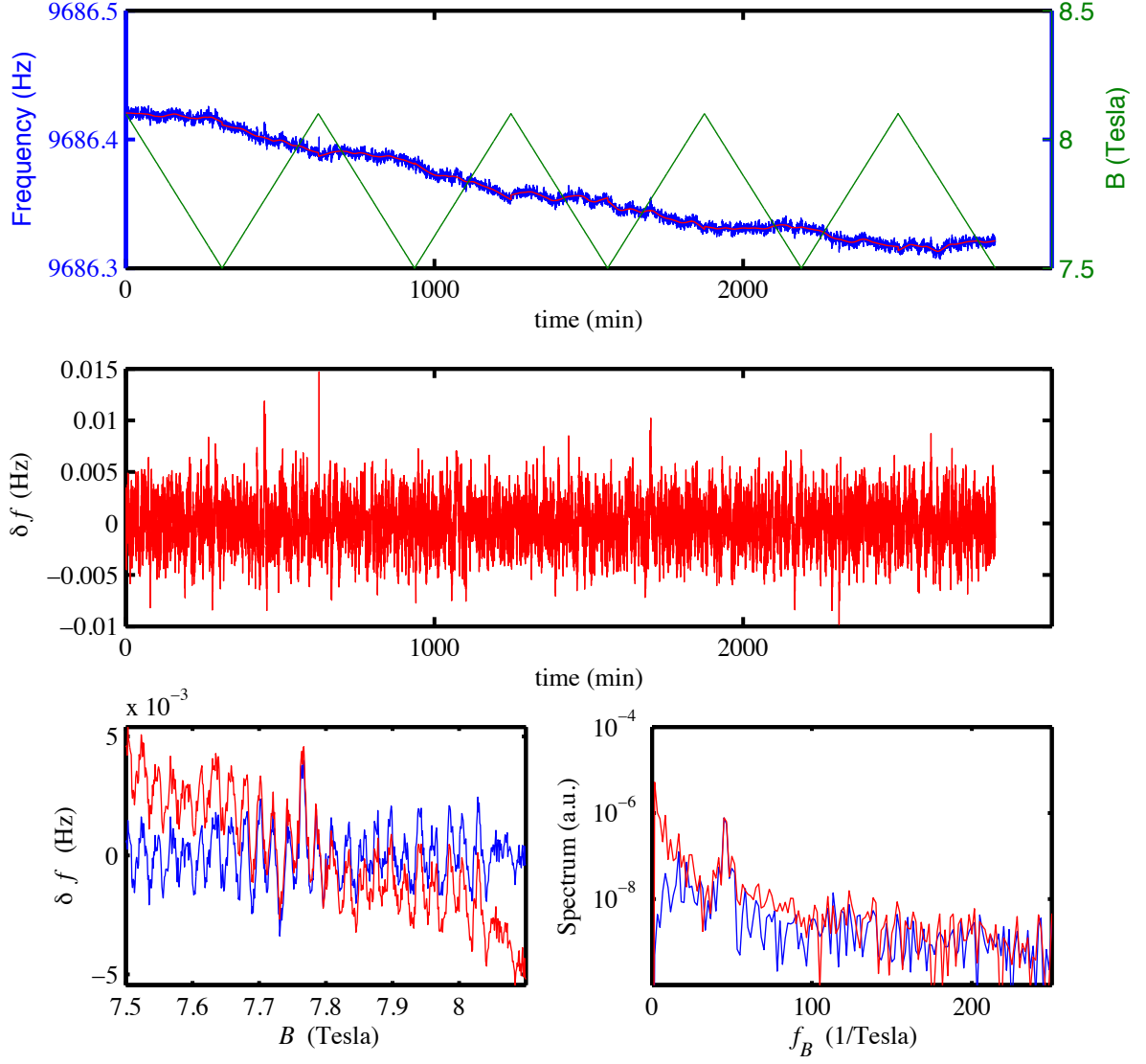
8

Figure 5: (a) Cantilever frequency (blue left axis) as the magnetic field (green right axis) is varied for sample 2. In this case, the time dependent background is so large, it is hard to distinguish the AB oscillations even after removing the drift as shown in (b). (c) The AB oscillations can be easily distinguished after averaging all the data with the drift (red) and with the drift substracted (blue). This proves that the observed oscillations are not an artifact of the procedure used to remove the drift. (d) Spectral density of (c) showing that the procedure used to remove the drift does not affect the amplitude of the observed oscillations.

## 2.2 Hilbert Transform

The Hilbert transform of a function $u(t)$ is defined as:

$$\text{p.v.} \frac{1}{\pi t} \otimes u(t) = H[u(t)] \equiv \hat{u}(t)$$

where p.v. is the Cauchy principal value and $\otimes$ indicates convolution. The Bedrosian

9

theorem states that the Hilbert transform acting on the product of two functions $x(t) = A(t) \times h(t)$ can be written as

$$H[A(t)h(t)] = A(t)H[h(t)] \tag{10}$$

if the Fourier spectra for $A(t)$ and $h(t)$ are disjoint in frequency space and if the spectrum for $h(t)$ is concentrated at higher frequencies than those of $A(t)$. For example, if $h(t)$ is a periodic function $h(t) = \cos\phi(t)$, $\hat{h}(t) = \sin\phi(t)$. In this regime, then the following relations hold (11):

$$x(t) = A(t)\cos\phi(t) \tag{11}$$

$$A(t) = \text{abs}(x(t) + i\hat{x}(t)) \tag{12}$$

$$\phi(t) = \arg(x(t) + i\hat{x}(t)) \tag{13}$$

For the work described in this paper, the Hilbert transform is used to analyze two separate data sets. In the first case, the Hilbert transform is applied to raw interferometer data (i.e. cantilever position vs. time). This technique allows us to generate densely sampled frequency vs. time traces, which are used to diagnose the sources of noise in the measurement. We discuss this technique in section 2.2.1. In the second case, the Hilbert transform is used to extract the persistent current quadrature amplitudes $I_{h/e}^{\pm}$ from the persistent current data. This is discussed in section 2.2.2.

### 2.2.1 Phase Noise Analysis

As explained in Ref. (2), the persistent current measurement is at its core a frequency ($f$) measurement of a driven cantilever. In order to better understand the specific noise sources of the measurement system, it is beneficial to have access to the noise spectral density $S_f(\omega)$ of raw frequency data $f(t)$

$$S_f(\omega) = 2\lim_{T\to\infty} \frac{|F_T(\omega)|^2}{T}$$

where $F_T(\omega)$ is the windowed fourier transform of $f(t)$

$$F_T(\omega) = \int_{-T/2}^{T/2} dt' f(t) e^{i\omega t'}$$

The factor of 2 comes from the fact that we are only considering single-sided spectral densities (thus we only consider $\omega > 0$ values). For the work described in the main text, we utitlize a technique involving the Hilbert transform to measure the frequency $f(t)$. The Hilbert transform is applied to cantilever position data obtained by an optical-fiber interferometer.

If the interferometer data contains more than one frequency component, we can define an "instantaneous frequency" $f(t) = f_0 + f_{noise}(t)$. Here $f_{noise}(t)$ is a stochastic variable with zero mean and $f_0$ is a constant. We will consider the limit in which the Fourier transform of the cantilever position is sharply peaked at $f_0$ and also $f_0 \gg \Delta f$, where $f_0$ is the center frequency and $\Delta f$ is the width of the peak. In this limit, the Bedrosian theorem (Eq. 10) holds, and we can use the Hilbert transform to calculate the cantilever phase vs. time with Eq. 13.

10

We convert the phase versus time $\phi(t)$ of the cantilever's motion to an instantaneous frequency $f(t)$ via the relationship:

$$2\pi f(t) = \frac{d\phi}{dt} \tag{14}$$

The frequency noise spectrum is related to the phase noise spectrum by $S_f = (\omega/2\pi)^2 S_\phi$ by Eq. (14). We can then compare the measured $S_f$ to theoretical predictions for the frequency noise of a driven limit-cycle oscillator subject to a white force noise and a white displacement noise in the detection (10)

$$S_{f,\,\text{thermal}}(\omega) = \frac{f_0 k_B T}{\pi k Q x_{\text{tip}}^2}$$
$$S_{f,\,\text{detector}}(\omega) = \frac{2 S_x^{\text{imp}}}{x_{\text{tip}}^2} \left(\frac{\omega}{2\pi}\right)^2 \tag{15}$$

where $k$ is the resonator spring constant, $Q$ is the resonator quality factor, $x_{\text{tip}}$ is the resonator displacement amplitude, and $S_x^{\text{imp}}$ is the displacement noise of the detector. The imprecision $S_x^{\text{imp}}$ in the measurement of the cantilever's motion arises from fluctuations both in the laser used to monitor the cantilever and in the detector used to measure the laser signal. The dominant noise source in our case is the electronic noise from the photoreciver. In order to convert the voltage at the output of the photodetector into cantilever motion, we measure this voltage when the cantilever is only excited by a thermal force. The magnitude of the cantilever's thermal motion can be computed from the equipartition theorem which states that at thermal equilibrium

$$k \left\langle x^2 \right\rangle = k_B T \tag{16}$$

The spectrum of the voltage $S_V$ at the output of the photodectector has the shape of lorentzian curve on top of an offset (inset of Figure 6). This offset consists of the measurement imprecision $S_x^{\text{imp}}$. By measuring $S_V$ at different temperatures (Figure 6), we can properly convert the volts at the output of the detector into displacement of the cantilever and calculate the imprecision $S_x^{\text{imp}}$ of our detector.

In these measurements, for some cantilevers, we notice a strong deviation from the prediction at low frequencies. This low-frequency behavior seems to correlate with the amount of mechanical nonlinearity in the cantilever (determined, e.g., by a non-Lorentzian resonance for large $x_{\text{tip}}$). For samples 3-8, there was very little nonlinearity and the frequency noise behaves as expected (Fig. 7). For samples 1 and 2, we noticed a large amount of mechanical nonlinearity and also a large amount of low-frequency noise (Fig. 8).

### 2.2.2 Calculating the Persistent Current Amplitude

The goal of the work in the main text is to measure the statistics of the quadrature amplitudes of the AB oscillations $I_{h/e}^{\pm}$. This amplitude slowly changes due to the magnetic field that penetrates the metal of the ring (3). Since our data is dominated by the first harmonic of Eq. 7 (no higher harmonics are visible in the data) the normalized derivative of the current $I'$ (Eq. 9) takes the form:

$$I'(B) = I_{h/e}^{+} \cos(2\pi p \frac{\phi}{\Phi_0}) - I_{h/e}^{-} \sin(2\pi p \frac{\phi}{\Phi_0}) \tag{17}$$
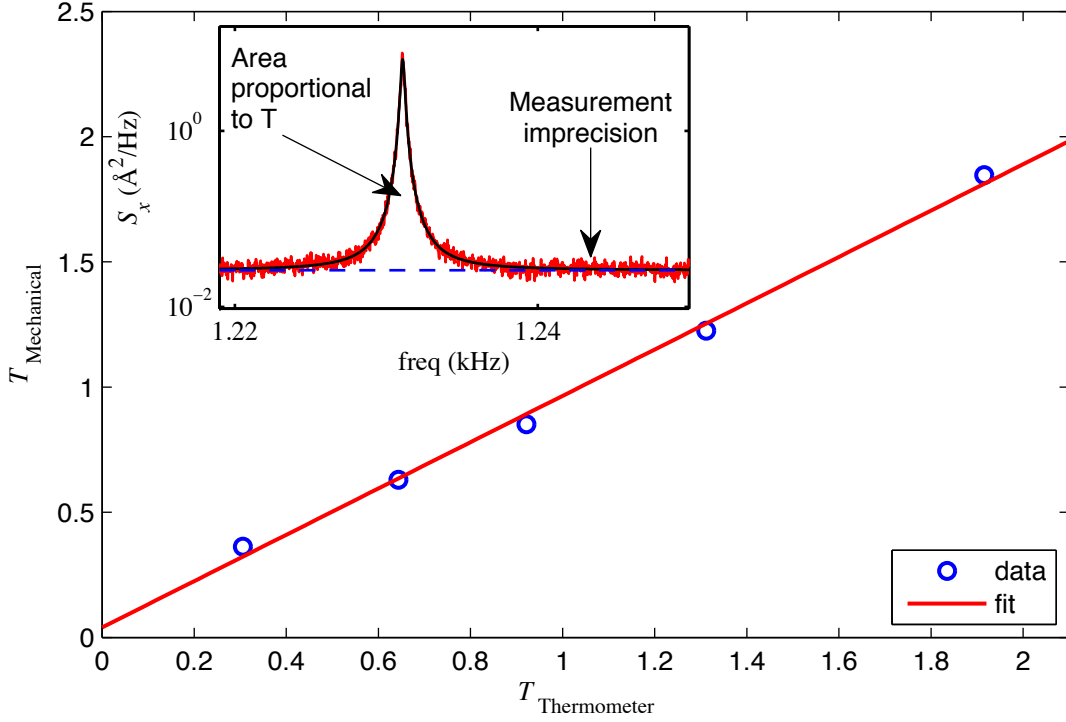$$= I_{h/e}(B) \cos\left(2\pi p \frac{B A \sin\theta}{\Phi_0} + \alpha(B)\right) \tag{18}$$

Figure 6: Thermal motion of the cantilever in units of temperature (Eq. 16) as a function of the fridge temperature. This motion is measured as a voltage at the output of the photodetector and converted into displacement units (inset). The spectral density of the voltage has two constributions: a white background that consists of the measurement imprecision $S_x^{\text{imp}}$ coming from the voltage noise of our photodetector (dashed blue line in the inset) , and a lorentzian curve that consists of the thermal motion of the cantilever. Measuring the detector's voltage fluctuations at different temperatures allows us to calibrate the intereferometer response.
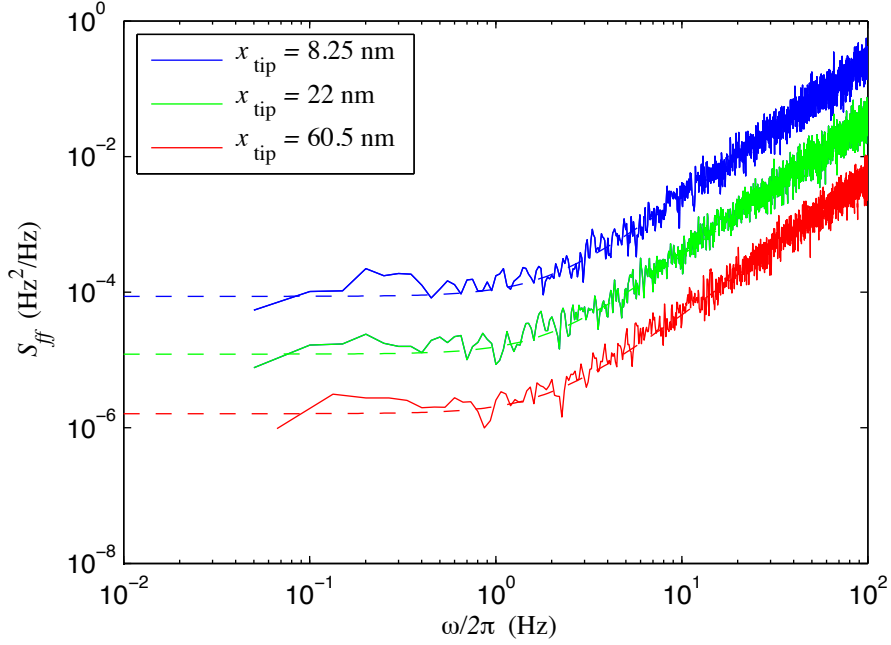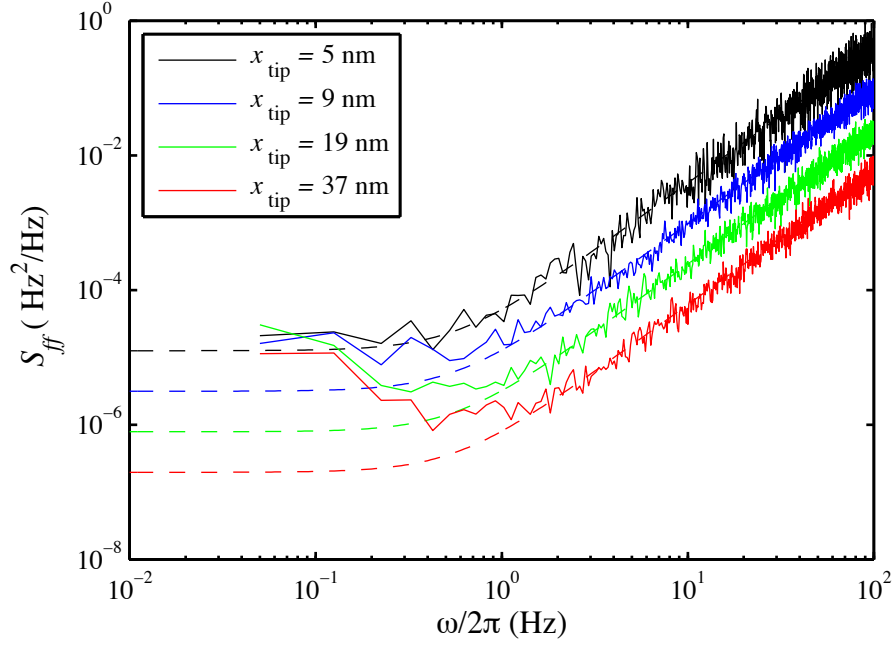
Figure 7: Frequency noise for sample 4. The solid lines represent the frequency noise spectrum data obtained using the Hilbert transform technique described above at various oscillator drive strengths. The dashed lines are the theoretical noise curves calculated with Eq. 15 (no fit parameters). There are two major contributions to the noise: thermal fluctuations driving the cantilever, and the intrinsic detector noise. The detector noise was extracted from the actual interferometer noise. For this cantilever, $Q = 5700$, $T = 320\,\text{mK}$, $f_0 = 966\,\text{Hz}$ and $k_L = 4.0 \times 10^{-5}\,\text{N/m}$.

Figure 8: Frequency noise for sample 2. The solid lines represent the frequency noise spectrum data obtained using the Hilbert transform technique described above at various oscillator drive strengths. The dashed lines are the theoretical noise curves calculated with Eq. 15 (no fit parameters). This sample exhibited strongly nonlinear behavior and its low-frequency noise deviates from the theoretical curves. For this cantilever, $Q = 35000$, $T = 320\,\mathrm{mK}$, $f_0 = 11827\,\mathrm{Hz}$ and $k_L = 1.7 \times 10^{-3}\,\mathrm{N/m}$.
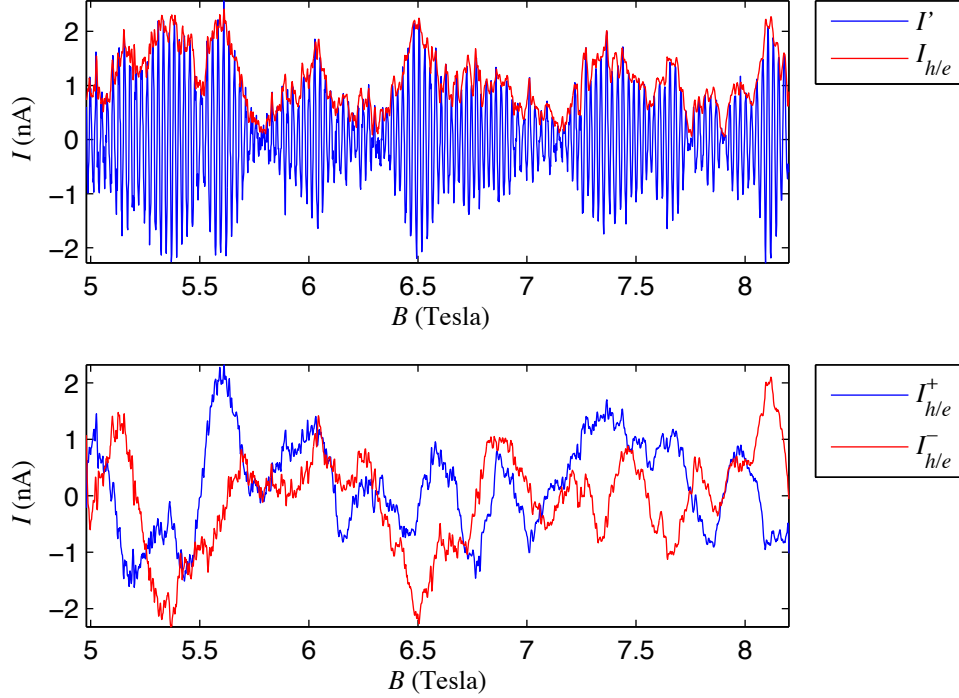
Figure 9: (a) Hilbert transform for the data from sample 6. From this trace we obtain $I_{h/e}(B)$ and $\alpha$ (not shown). (b) Using the data from (a) we can infer the values for $I_{h/e}^{+}$ and $I_{h/e}^{-}$.

where $I_{h/e}(B)$ is the amplitude of the current and $\cos\left(2\pi p \frac{BA\sin\theta}{\Phi_0} - \alpha(B)\right)$ represents the AB oscillations.

The correlation field $B_c$ sets the field scale over which $I_{h/e}(B)$ changes. In the limit that $B_c$ is "large enough" $(B_c \gg \Phi_0/A)$, $I_{h/e}(B)$ is a slowly-varying function compared to $\cos(2\pi p \frac{BA\sin\theta}{\Phi_0} - \alpha)$ and the Bedrosian theorem (10) holds. The AB frequency is also sharply peaked in Fourier space, with a well-defined frequency given by the dimensions of the ring. Thus, comparing (12) and (17), we can obtain $I_{h/e}(B)$ and $\alpha$ using the Hilbert transform. This also allows us to determine the quadrature variables $I_{h/e}^{+} = I_{h/e}\cos(\alpha)$ and $I_{h/e}^{-} = I_{h/e}\sin(\alpha)$. This technique is illustrated in Fig. 9.

## 2.3   Definition of the cumulants and statistical moments

For the purpose of this manuscript, it is convenient to have a consistent definition of the various moments and cumulants. The raw moments $\mu'_r$ and central moments $\mu_r$ of a stochastic variable $x$ are defined as

$$
\begin{aligned}
\mu'_r &= \langle x^r \rangle \\
\mu_r &= \left\langle \left(x - \mu'_1\right)^r \right\rangle
\end{aligned}
\tag{19}
$$

The cumulants $\langle\langle I^n \rangle\rangle$ are most easily defined in terms of the central moments:

$$
\begin{aligned}
\langle\langle I^2 \rangle\rangle &= \mu_2 \\
\langle\langle I^3 \rangle\rangle &= \mu_3
\end{aligned}
$$

$$\langle\langle I^4 \rangle\rangle = \mu_4 - 3\mu_2^2 \tag{20}$$
$$\langle\langle I^5 \rangle\rangle = \mu_5 - 10\mu_3\mu_2$$
$$\langle\langle I^6 \rangle\rangle = \mu_2 - 15\mu_4\mu_2 - 10\mu_3^2 + 30\mu_2^3$$

## 2.4 Finite sample statistics

In Ref. (3) it was mentioned that in the presence of an additional large in-plane magnetic field $B_m$ penetrating the metal ring, the effective disorder of the ring changes, implying that averaging over magnetic field is equivalent to an ensemble average (4). However, our finite magnetic field range means that in practice, we have a finite number of realizations from this ensemble. In order to estimate the statistical uncertainty in our estimates of the cumulants due to this finite sample size, we use the results of Ref. (5).

The statistical uncertainty of the cumulants ($\langle\langle I^n \rangle\rangle$) due to a finite sample size can be expressed in terms of the normalized correlation function $C(x)$ defined as

$$C\left(\frac{B - B'}{B_c}\right) = \frac{\langle I(B)I(B') \rangle}{\langle I^2 \rangle}$$

where $C$ decays from $C(0) = 1$ to $C(\infty) = 0$, and $B_c$ is the correlation field, which sets a rough order of magnitude over which the persistent current is correlated. Expressions for $C$ are provided in Ref. (3). The typical value of a cumulant calculated from a finite ensemble is given by

$$\left\langle \langle\langle I^n \rangle\rangle^2 \right\rangle_B = \langle\langle I^n \rangle\rangle^2 + a_n \frac{B_c}{B_{\mathrm{span}}} \langle\langle I^2 \rangle\rangle^n$$

where $a_n = n! \int_{-\infty}^{\infty} [C(x)]^n dx$, and $B_{\mathrm{span}}$ is the total magnetic field range over which data is taken. The theoretical prediction for the higher order cumulants of the persistent current quadratures is

$$\langle\langle I^n \rangle\rangle \sim \frac{I_{\mathrm{typ}}^n}{g^{n-2}}$$

for $n > 2$, where the typical current is defined as $I_{\mathrm{typ}} = \sqrt{\langle I^2 \rangle}$ (1). In our case $g \sim 10^4$ and thus we expect a gaussian distribution for $I_{h/e}^{\pm}$ and the statistical error is thus given by

$$\delta \langle\langle I^n \rangle\rangle = \sqrt{a_n \frac{B_c}{B_{\mathrm{span}}} \langle I^2 \rangle^n} \tag{21}$$

For an estimate of this term, we can consider the case for a spinless electron at $T = 0$ and large $B_m$ (so that we can ignore the Cooperon contribution) and only include the first harmonic of the PC. In this case

$$C(x) = \left(1 + |x| + \frac{x^2}{3}\right) e^{-|x|} \tag{22}$$

For this simplified case, the first 4 coefficients are $a_2 = 7$, $a_3 = 16.61$, $a_4 = 56.48$, and $a_5 = 249.55$. Experimental values of the cumulants of the persistent currents are considered sound only if they comfortably exceed the systematic error $\sqrt{a_n \frac{B_c}{B_{\mathrm{span}}} \langle I^2 \rangle^n}$ (Eq. 21). The actual correlation function for our case is more complicated than Eq. 22 and is a function of $T$ and $L_{SO}$. It can be numerically implemented using Ref. (3). A fit to the correlation function $C(B/B_c, T, L_{SO})$ of our data is shown in Fig. 10.[3]

---

[3]The correlation function is a also a function of the Zeeman energy, but at the large magnetic fields used in this experiment, this dependence is negligible.
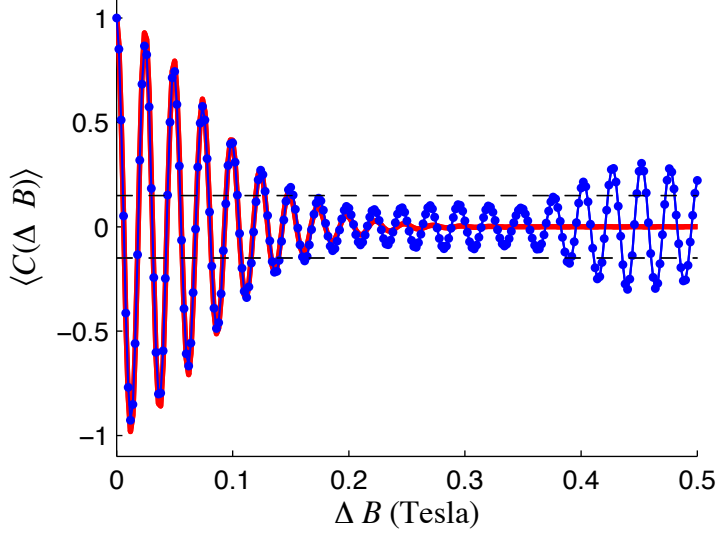
Figure 10: Persistent current autocorrelation for sample 6. Blue represents the autocorrelation of the data shown in Fig. 20 and red is the fit using Ref. (3). The estimated correlation field in this case is $B_c = 32$mT. In order to estimate the standard error in the autocorrelation (dashed horizontal lines), we assume that this is approximatly given by the standard error for the correlation coefficient $1/\sqrt{N_{\text{eff}}} \approx 0.15$. As it can be seen in the figure, fluctuations of this order are present at large $\Delta B \gg B_c$, where the autocorrelation of an infinitely large data set would be expected to vanish.

We can also define an effective number of samples based on the expected statistical uncertainty for the cumulants of an ensemble of $N_{\text{eff}}$ samples (12):

$$\delta \langle\langle I^n \rangle\rangle = \sqrt{\frac{n! \, \langle\langle I^2 \rangle\rangle^n}{N_{\text{eff}}}}.$$

By comparing the latter with Eq. 21, we can then define $N_{\text{eff}}$ as

$$N_{\text{n,eff}} = \frac{n! B_{\text{span}}}{a_n B_c}. \tag{23}$$

## 2.5 Finite signal to noise

Another source of error in our estimate of the cumulants is the finite sensitivity of our setup. In order to estimate this error, we have to calcualte the appropriate expression for error propagation in our analysis. Our case is somewhat confusing, since $x_i$ itself is an stochastic variable, so really we have $x_{i,meas} = x_i + \delta x_i$. First let's consider the general equation for the error propagation for a general function $f(x_1, x_2..., x_N)$. If $x_i$ is known only to within an error $\delta x_i$ then the error in $f$ is given by

$$\delta^2 f = \sum_i \left( \frac{\partial f}{\partial x_i} \delta x_i \right)^2 \tag{24}$$

Let's first consider the case of the central moment as cumulants are easily definined in terms of them:

$$f(x_i) = \mu_r = \frac{1}{N} \sum_i \left( x_i - \mu_1' \right)^r$$

17

Then

$$\langle \delta^2 \mu_r \rangle \;=\; \left(\frac{r}{N}\right)^2 \sum_i \left(x_i - \mu_1'\right)^{2r-2} \langle \delta^2 x_i \rangle$$

$$\;=\; \frac{r^2}{N} \mu_{2r-2} \langle \delta^2 x \rangle \tag{25}$$

There are two assumptions used for Eq. 25. First, we assume that the noise $\delta x_i$ from the different magnetic field points (labeled with the index $i$) are uncorrelated. This **does not** mean that the different $x_i$'s are uncorrelated. The second assumption is that $\delta^2 x_i$ can be replaced by an average $\delta^2 x$. Although not completely accurate, since the sensitivity of our measurement is lower at lower magnetic fields, we did compensate for the loss of sensitivity by averaging longer at low magnetic fields.

The expressions for the second and third cumulants are the same as for the second and third central moments. Thus, Eq. 25 gives their measurement uncertainty. For the forth, fifth and sixth cumulant we can use the following heuristic approach (12). We start with the definition of the cumulants (Eq. 20), from which the following expressions are derived:

$$\delta \langle\langle I^4 \rangle\rangle \;=\; \delta\mu_4 - 6\mu_2\delta\mu_2$$
$$\delta \langle\langle I^5 \rangle\rangle \;=\; \delta\mu_5 - 10\mu_2\delta\mu_3 - 10\mu_3\delta\mu_2$$
$$\delta \langle\langle I^6 \rangle\rangle \;=\; \delta\mu_6 - 15\mu_4\delta\mu_2 - 15\mu_2\delta\mu_4 - 20\mu_3\delta\mu_3 + 90\mu_2^2\delta\mu_2$$

Then, for example, for the fourth cumulant:

$$\langle \delta^2 \langle\langle I^4 \rangle\rangle \rangle = \delta^2\mu_4 + 36\mu_2^2\delta^2\mu_2 - 12\mu_2 \langle \delta\mu_4\delta\mu_2 \rangle \tag{26}$$

The covariance $\langle \delta\mu_4\delta\mu_2 \rangle$ is not necessarily zero and it can be derived using a similar approach as the one used to derive Eq. 25:

$$\langle \delta\mu_r\delta\mu_s \rangle = \frac{rs}{N} \mu_{r+s-2} \langle \delta^2 x \rangle$$

Similar expressions to Eq. 26 for $\langle\langle I^5 \rangle\rangle$ and $\langle\langle I^6 \rangle\rangle$ can be derived.

## 2.6   Data

Following, we show a table with all the estimated cumulants and estimated errors for the cumuluants of all 8 samples. The cumulants of both $I^+$ and $I^-$ have been combined for each of the rings. In order to account for variations between rings the different cumulants are normalized by the variance $\langle\langle I^2 \rangle\rangle$; thus we define a normalized cumulant $\kappa_n \equiv \langle\langle I^n \rangle\rangle / \langle\langle I^2 \rangle\rangle^{n/2}$.

| Sample # | $r$ (nm) | $B_c$ (mT) | $N_{2,\text{eff}}$ | $\left\langle\!\left\langle (I^{\pm})^2 \right\rangle\!\right\rangle$ (nA$^2$) | $\kappa_3$ |
|---|---|---|---|---|---|
| 1 | 296 | $16 \pm 1$ | 63 | $0.46 \times (1 \pm 0.18 \pm 0.02)$ | $0.065 \pm 0.28 \pm 0.05$ |
| 2 | 296 | $25 \pm 1.5$ | 43 | $0.37 \times (1 \pm 0.22 \pm 0.02)$ | $0.23 \pm 0.34 \pm 0.04$ |
| 3 | 448 | $9 \pm 1$ | 55 | $0.0031 \times (1 \pm 0.2 \pm 0.03)$ | $0.21 \pm 0.31 \pm 0.08$ |
| 4 | 448 | $17 \pm 1$ | 34 | $0.0063 \times (1 \pm 0.24 \pm 0.02)$ | $-0.25 \pm 0.4 \pm 0.07$ |
| 5 | 296 | $22 \pm 1$ | 56 | $0.597 \times (1 \pm 0.19 \pm 0.01)$ | $0.18 \pm 0.29 \pm 0.03$ |
| 6 | 296 | $32 \pm 2$ | 44 | $0.67 \times (1 \pm 0.21 \pm 0.01)$ | $0.001 \pm 0.34 \pm 0.02$ |
| 7 | 296 | $20 \pm 1$ | 81 | $0.26 \times (1 \pm 0.16 \pm 0.01)$ | $0.083 \pm 0.24 \pm 0.03$ |
| 8 | 418 | $11 \pm 1$ | 36 | $0.022 \times (1 \pm 0.23 \pm 0.02)$ | $-0.05 \pm .37 \pm 0.05$ |

| Sample # | $\kappa_4$ | $\kappa_5$ | $\kappa_6$ |
|---|---|---|---|
| 1 | $-0.052 \pm 0.51 \pm 0.1$ | $-0.12 \pm 1.1 \pm 0.25$ | $-0.91 \pm 2.6 \pm 0.47$ |
| 2 | $-0.0271 \pm 0.62 \pm 0.07$ | $-0.83 \pm 1.3 \pm 0.2$ | $-0.93 \pm 3.1 \pm 0.41$ |
| 3 | $0.29 \pm 0.58 \pm 0.18$ | $-0.05 \pm 1.23 \pm 0.5$ | $-0.84 \pm 2.9 \pm 1.13$ |
| 4 | $0.56 \pm 0.75 \pm 0.16$ | $0.27 \pm 1.58 \pm 0.5$ | $-0.043 \pm 3.7 \pm 1.32$ |
| 5 | $-0.25 \pm 0.54 \pm 0.04$ | $-0.17 \pm 1.15 \pm 0.14$ | $0.36 \pm 2.7 \pm 0.28$ |
| 6 | $-0.61 \pm 0.637 \pm 0.03$ | $-0.05 \pm 1.35 \pm 0.09$ | $2.23 \pm 3.15 \pm 0.18$ |
| 7 | $0.065 \pm 0.45 \pm 0.07$ | $0.51 \pm 0.95 \pm 0.23$ | $2.85 \pm 2.23 \pm 0.45$ |
| 8 | $0.2 \pm 0.68 \pm 0.086$ | $0.12 \pm 1.4 \pm 0.23$ | $-2.1 \pm 3.35 \pm 0.58$ |

Table 1: Higher order moments of the quadrature amplitudes of the persistent current for all the measured samples. The first error indicates the standard error due to finite-size sample and the other represents uncertainty from noise in the frequency measurement. $N_{2,\text{eff}}$ indicates the effective number of samples for a given ring using Eq. 23 multiplied by 2 as we use both quadratures $I^{\pm}$ to calculate the cumulants.

# 3   Measurement diagnostics

We performed a set of diagnostic measurements similar to those described in Ref. (2). Specifically, we measured the effects of the readout laser power on the measured frequency, we compared the extracted current using the two first modes of the cantilever motion and we checked the effects of cantilever oscillation amplitude.

Figures 11 and 12 show the effect of varying the laser power upon the persistent current data measured on two different cantilevers for different incident laser powers. For different cantilevers, we observed two qualitatively different types of dependence upon the laser power. We believe this difference is due to the different widths of the cantilevers. The data of samples 1-4 where taken with an incident power of 10 nW. However, for samples 5-7, the data was taken with an laser incident power of 3 nW as they presented a stronger power dependence. Sample 8 was taken with a laser power of 5 nW in a previous cooldown (Ref. (2)).

| Sample # | $r$ (nm) | $w$ (nm) | $t$ (nm) | $l_{\text{cantilever}}$ ($\mu$m) | $w_{\text{cantilever}}$ ($\mu$m) |
|---|---|---|---|---|---|
| 1 | 296 | 90 | 115 | 114 | 40 |
| 2 | 296 | 90 | 115 | 126 | 40 |
| 3 | 448 | 90 | 115 | 395 | 40 |
| 4 | 448 | 90 | 115 | 398 | 40 |
| 5 | 296 | 90 | 115 | 370 | 20 |
| 6 | 296 | 85 | 115 | 359 | 20 |
| 7 | 296 | 95 | 115 | 352 | 20 |
| 8 | 418 | 85 | 90 | 438 | 60 |

Table 2: Sample parameters. All the measurements were done at a 45-degree angle between the cantilever and ring plane and the magnetic field. All the cantilevers had a thickness of 118 nm except for sample 8 which had a thickness of 340 nm. Sample 8 was measured in a separate cooldown.

In Fig. 13 we demonstrate that the inferred current is the same whether the cantilever's first or second flexural mode is used, indicating that persistent current is independent of excitation frequency of the cantilever. Finally, in Fig. 14 we show that the cantilever's frequency depends upon the amplitude of its motion as would be expected if the persistent current remains in its equilibrium state (Eq. 8). To generate the data shown in Fig. 14, the resonant frequency of cantilever 5 was measured at two different magnetic fields (indicated in the inset figure with two arrows) as a function of cantilever amplitude $x_{\text{tip}}$. Then, the two measured $\delta f$ were substracted in order to remove any kind of amplitude-dependent change in the cantilevers resonance frequency. The cantilever was excited in its first flexural mode.
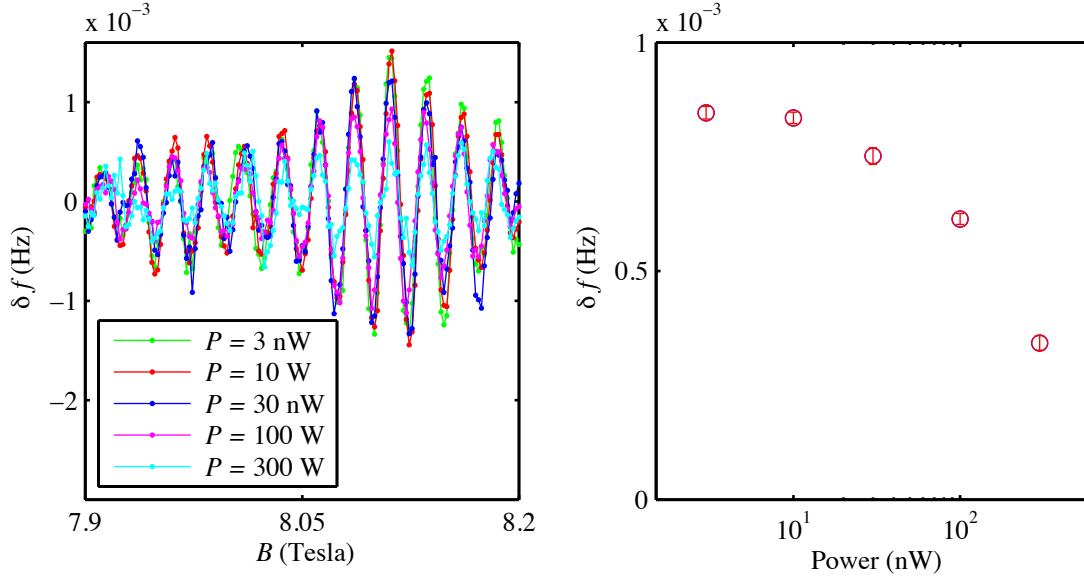


Figure 11: Left panel: Change in frequency versus magnetic field for a series of laser powers incident on the cantilever. This data was taken with sample 6. The drive was the same for all the traces. Right panel: The mean amplitude of each of the traces from the left panel, plotted versus laser power. For the data of samples 5, 6 and 7 shown in the main paper, 3 nW of laser power was used.
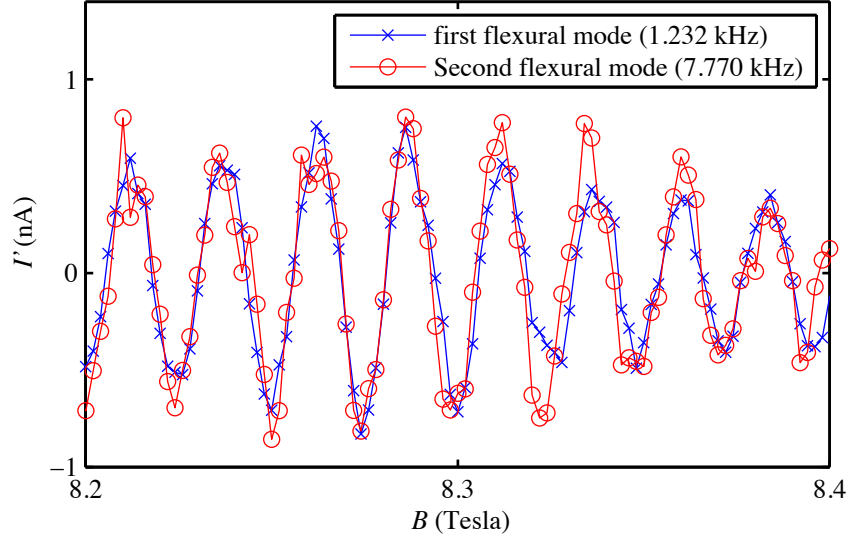
Figure 13: The derivative of the persistent current I´ (derived from Eqs. 8 and 9) versus magnetic field measured when oscillating the cantilever at 1.232 kHz (the cantilever's first flexural resonance) and at 7.77 kHz (the cantilever's second flexural resonance). The persistent current does not appear to depend on the cantilever oscillation frequency.
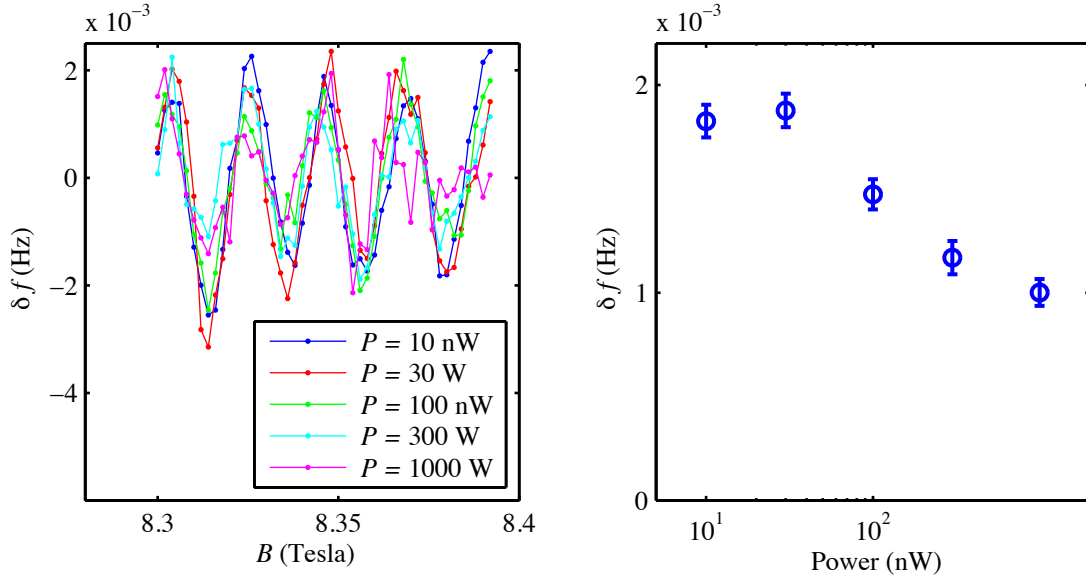


Figure 12: Left panel: Change in frequency versus magnetic field for a series of laser powers incident on the cantilever. This data was taken with sample 2. The drive was the same for all the traces. Right panel: The mean amplitude of each of the traces from the left panel, plotted versus laser power. For the data of samples 1, 2, 3 and 4 shown in the main paper, 10 nW of laser power was used.
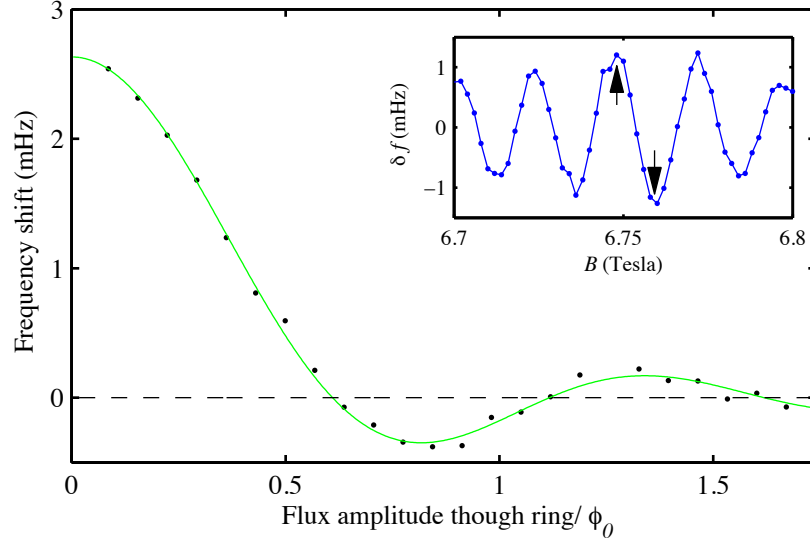
Figure 14: Cantilever drive test on sample 5 where we measure the accuracy of Eq. 8. The cantilever amplitude is plotted on the $x$-axis in terms of the amplitude of the flux modulation $\phi_{ac}/\phi_0$ through the ring produced by the cantilever motion. Data points reperesent the difference in cantilever frequency shift for the two field values indicated in the inset. The solid curve is a fit using Eq. 8 (with $p = 1$) and $r = 301 \pm 2\,\mathrm{nm}$, consistent with the measured radius and linewidth of our ring (see table 2). Inset: the arrows indicate two field values at which measurements of the cantilever frequency shift were performed as a function of cantilever amplitude.

# 4  Data of all the samples

## 4.1  Magnetic field sweeps

In this last section, we present figures 15-22 where we show the complete $I'$ versus magnetic field traces which were analyzed in the main text. These traces were calculated, using method B of Ref. (2) from measurements of the cantilever frequency performed at the refrigerator's base temperature of 320 mK (365 mK for sample 8).
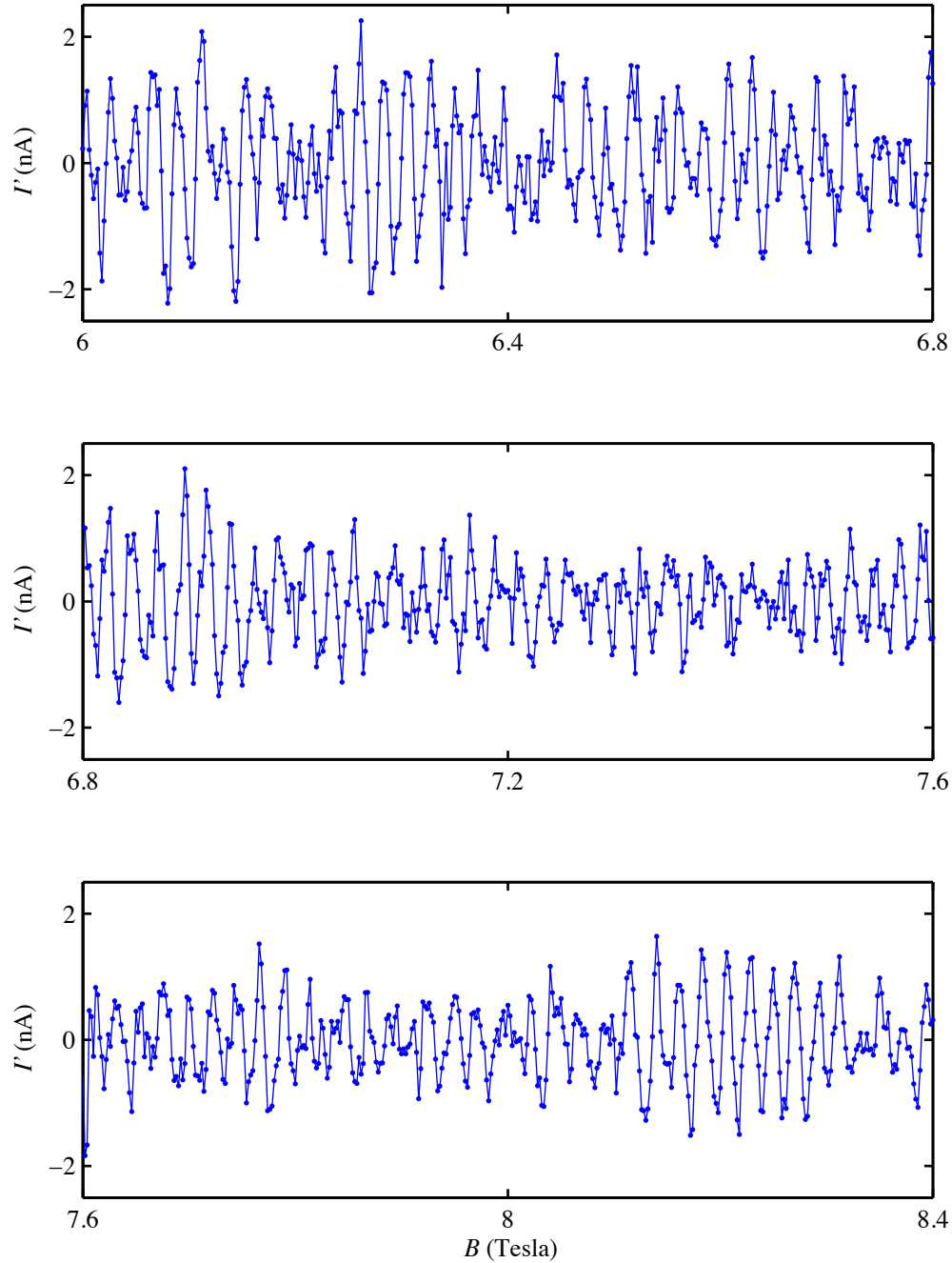


Figure 15: The derivative of the persistent current $I'$ (derived from Eqs. 8 and 9) versus magnetic field for sample 1 at T = 320 mK. The full sweep is separated into three contiguous panels for clarity.
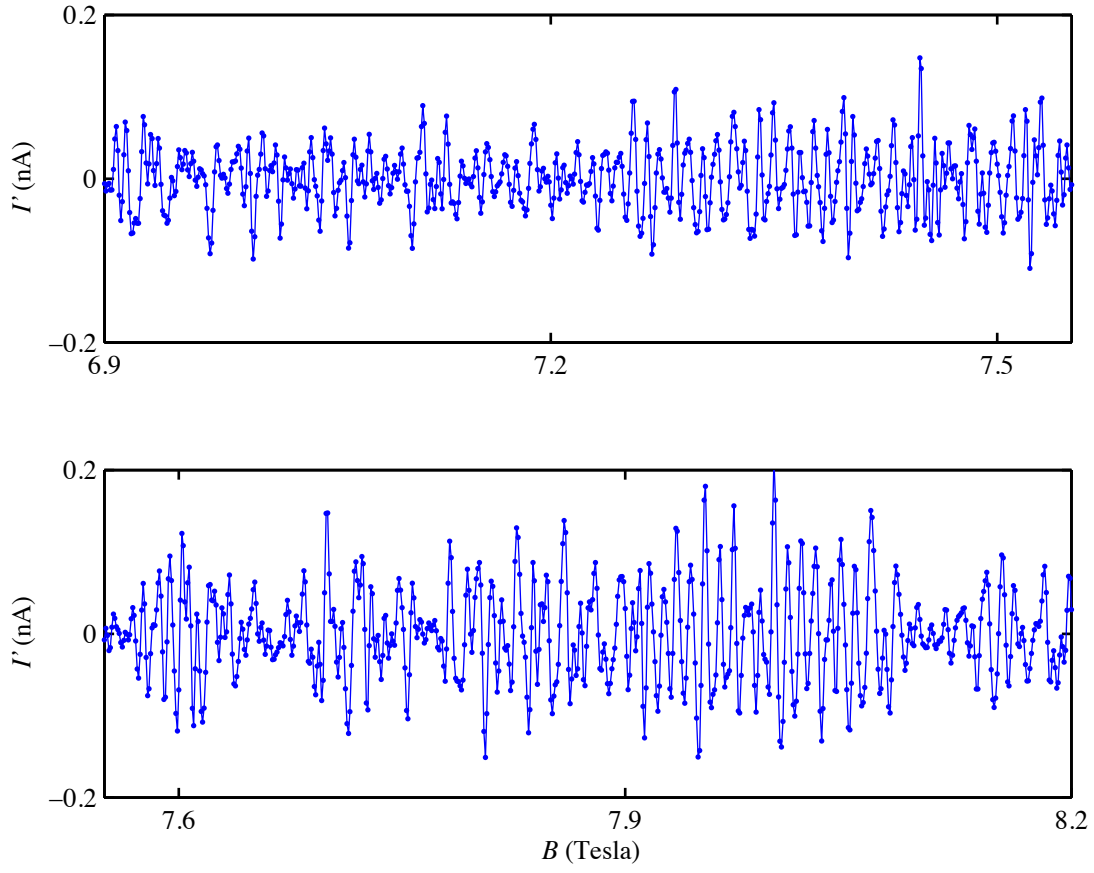
Figure 17: The derivative of the persistent current $I'$ (derived from Eqs. 8 and 9) versus magnetic field for sample 3 at T = 320 mK.
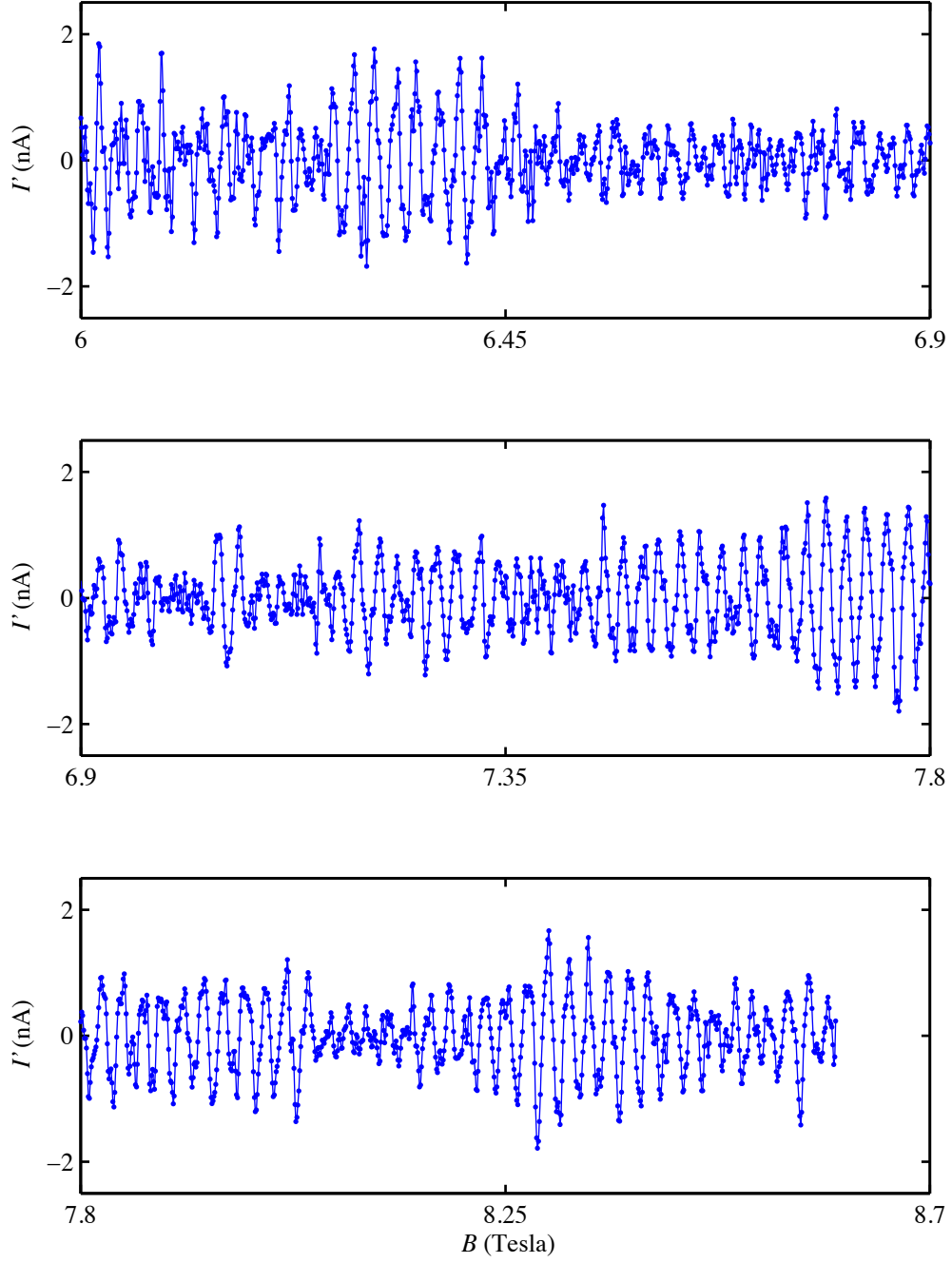
Figure 16: The derivative of the persistent current $I'$ (derived from Eqs. 8 and 9) versus magnetic field for sample 2 at T = 320 mK.
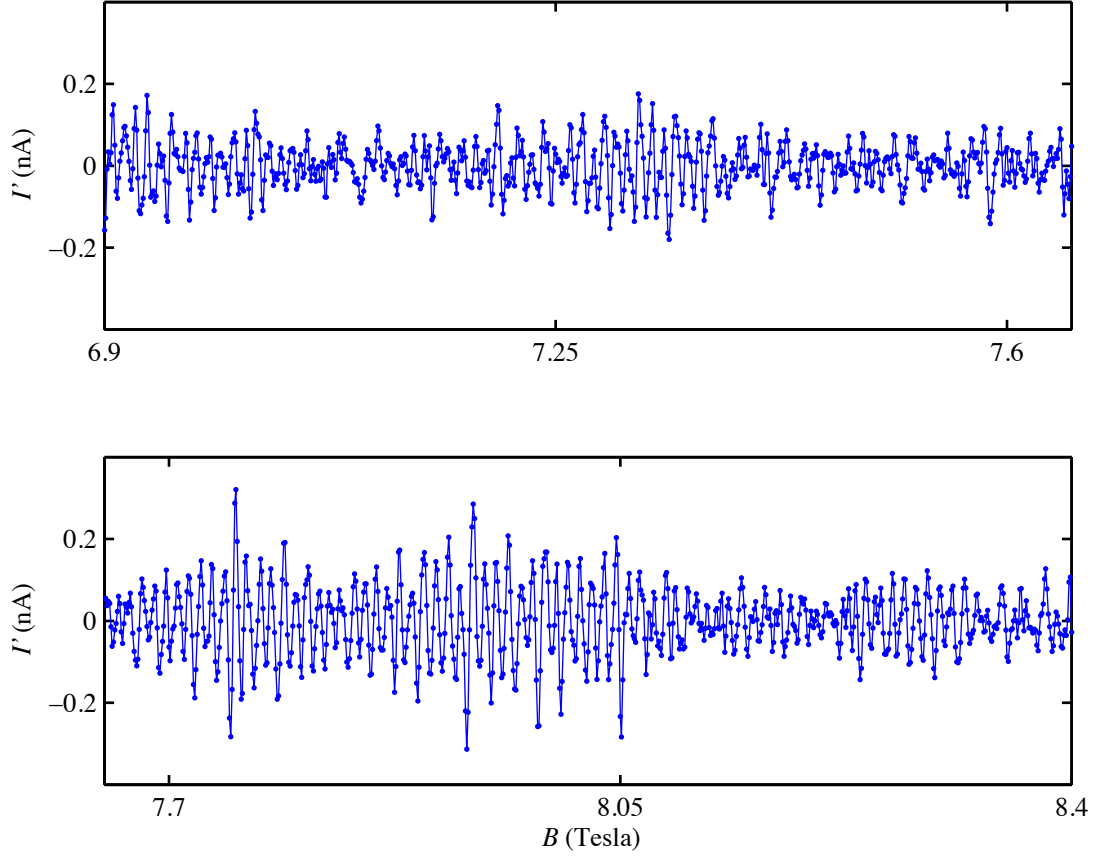
Figure 18: The derivative of the persistent current $I'$ (derived from Eqs. 8 and 9) versus magnetic field for sample 4 at T = 320 mK.
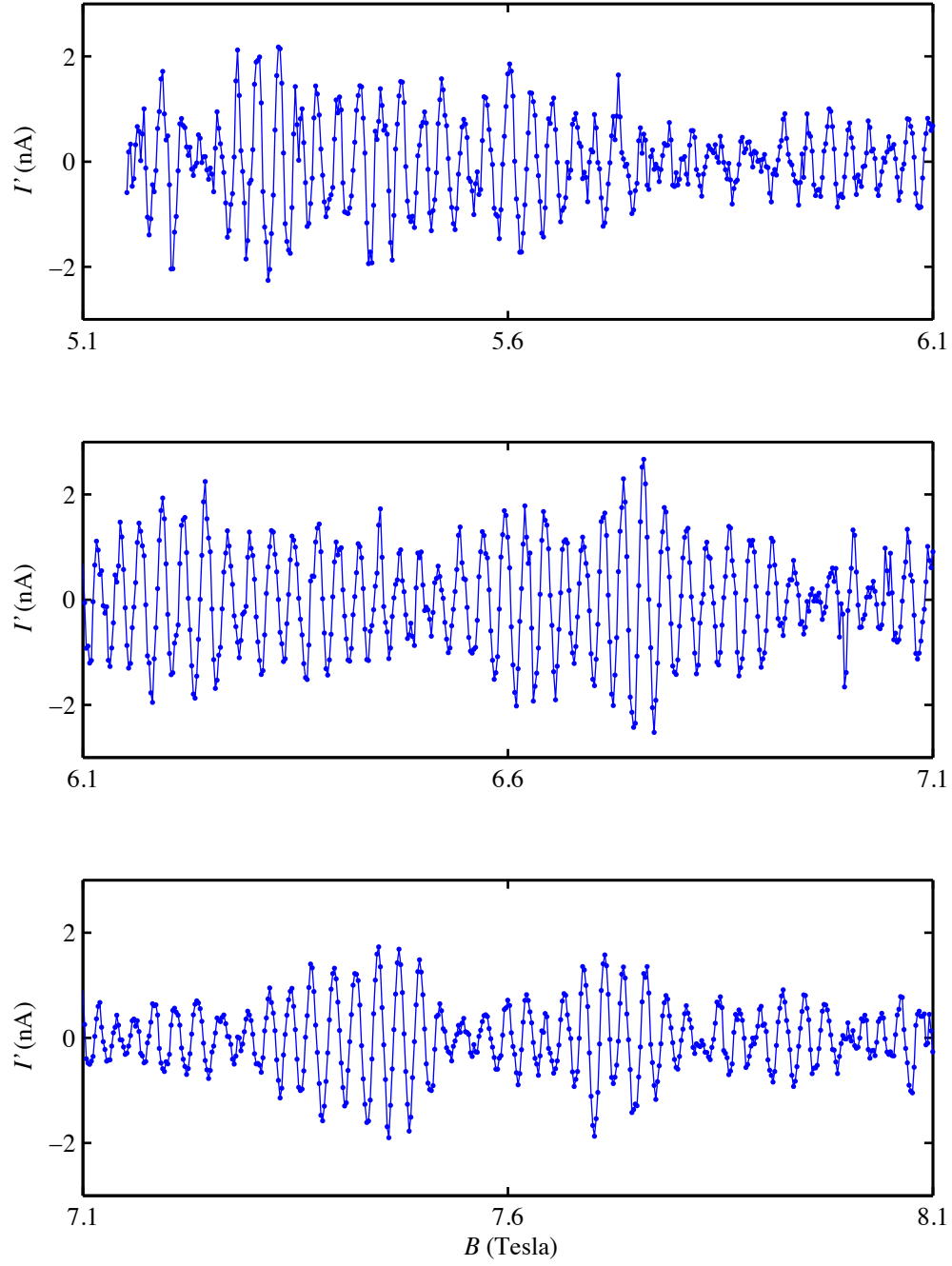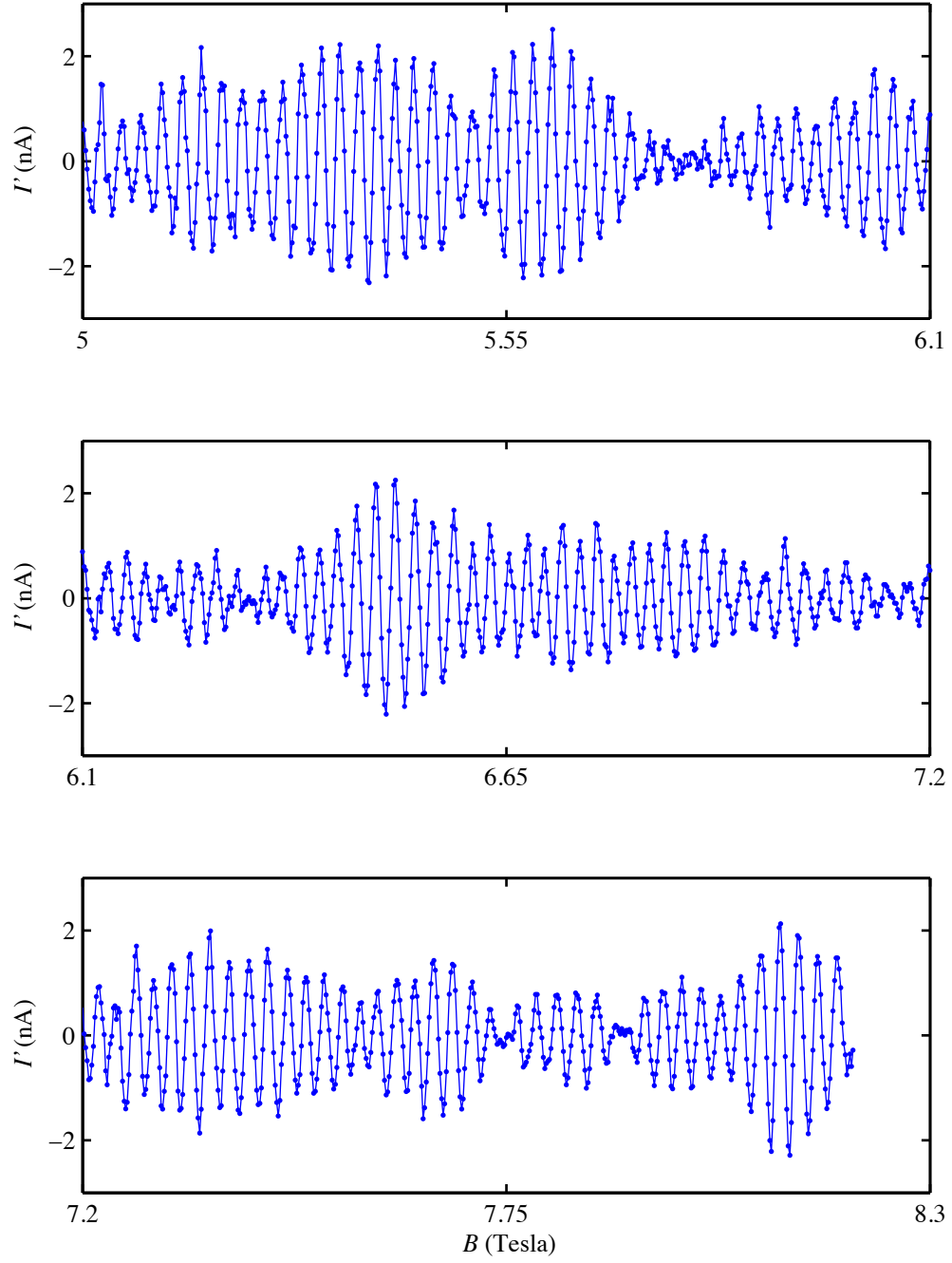
Figure 19: The derivative of the persistent current $I'$ (derived from Eqs. 8 and 9) versus magnetic field for sample 5 at T = 320 mK.

Figure 20: The derivative of the persistent current $I'$ (derived from Eqs. 8 and 9) versus magnetic field for sample 6 at T = 320 mK.
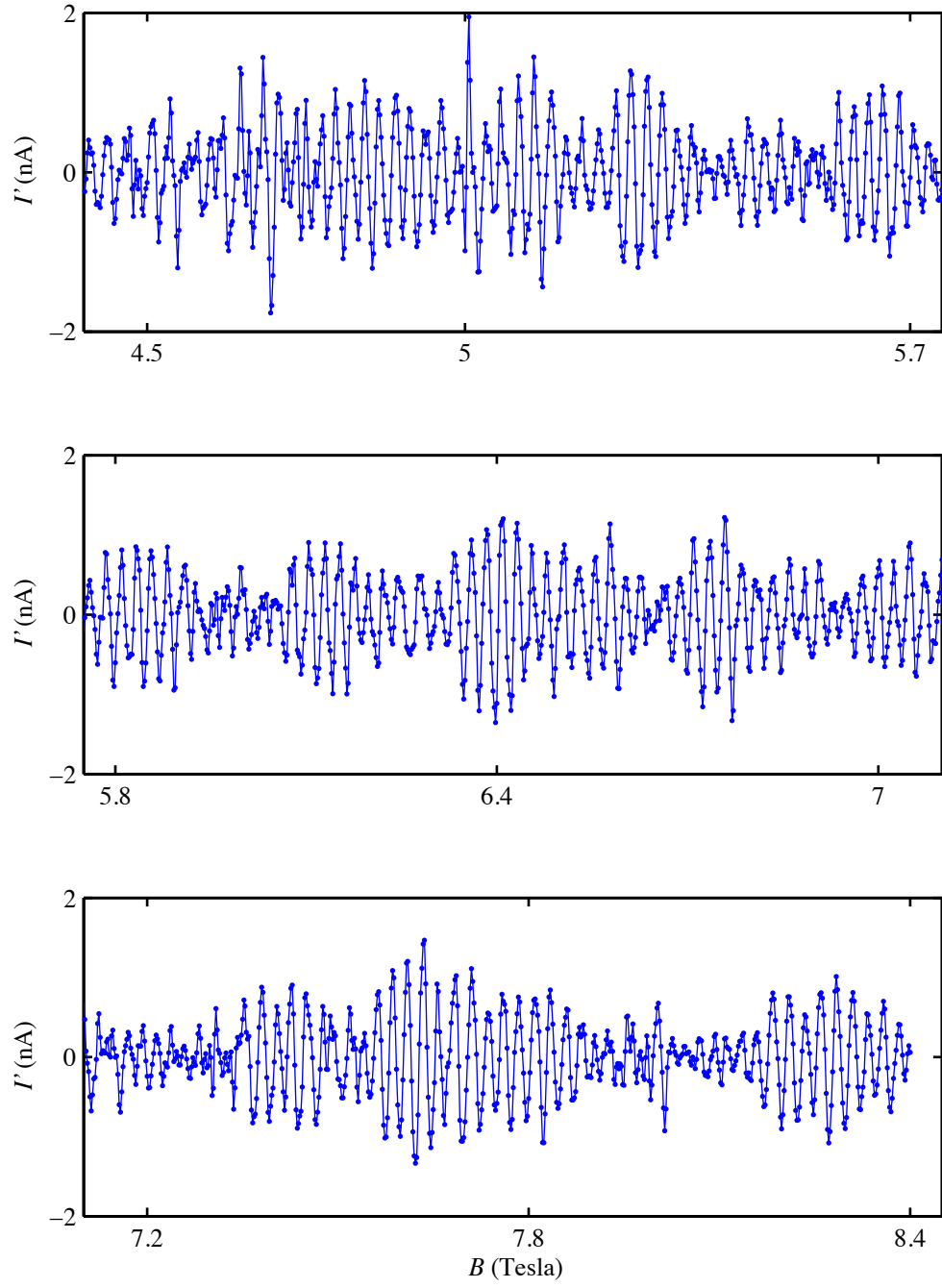
Figure 21: The derivative of the persistent current $I'$ (derived from Eqs. 8 and 9) versus magnetic field for sample 7 at T = 320 mK.
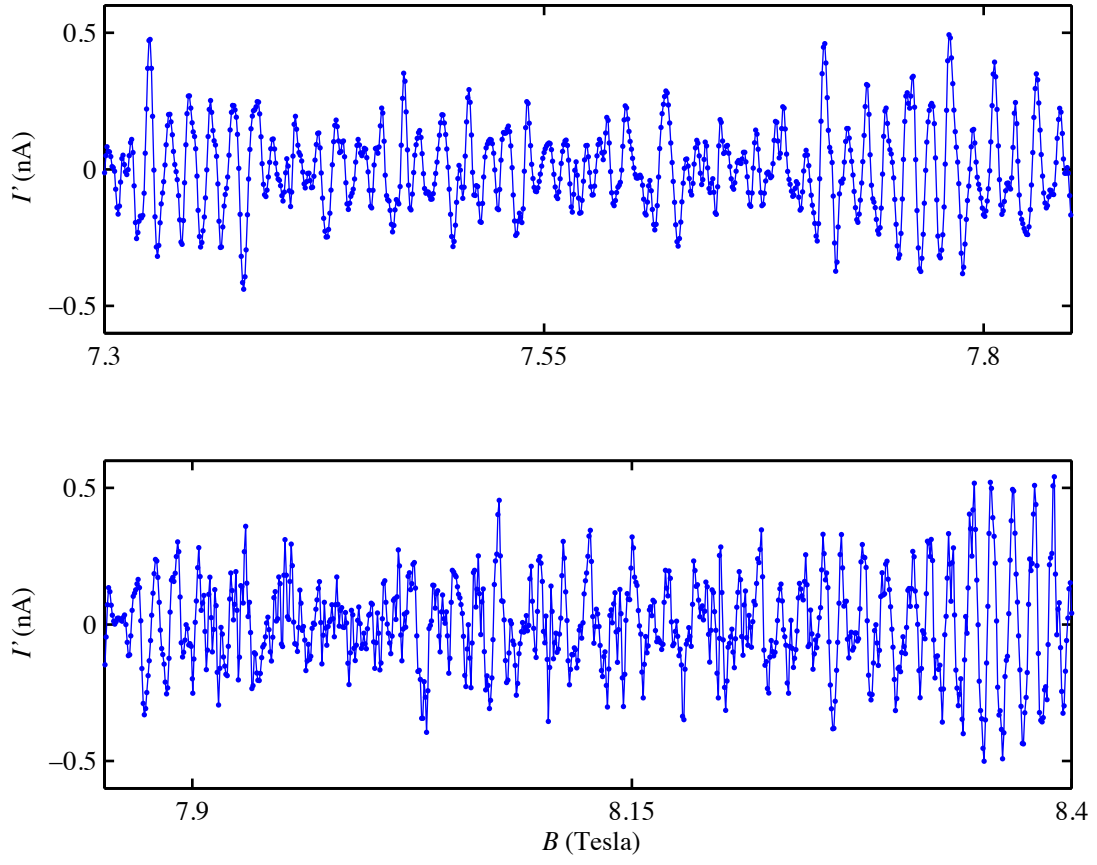
Figure 22: The derivative of the persistent current $I'$ (derived from Eqs. 8 and 9) versus magnetic field for sample 8 at T= 365 mK.

# References

[1] Houzet, M. Distribution function of persistent current. Physical Review B 82, 1–4 (2010).

[2] Bleszynski-Jayich, A. C. et al. Persistent currents in normal metal rings. Science (New York, N.Y.) 326, 272–5 (2009).

[3] Ginossar, E. et al. Mesoscopic persistent currents in a strong magnetic field. Physical Review B 81, 1–11 (2010).

[4] Lee, P. A. & Stone, A. D. Universal conductance fluctuations in metals. Physical Review Letters 55, 1622–1625 (1985).

[5] Tsyplyatyev, O., Aleiner, I., Fal'ko, V. & Lerner, I. Applicability of the ergodicity hypothesis to mesoscopic fluctuations. Physical Review B 68, 17–20 (2003).

[6] Chandrasekhar, V. Electron Quantum Interference in Small Metal Wires and Loops. Ph.D. thesis, Yale University (1989).

[7] Ashcroft, N. W. & Mermin, N. D. Solid State Physics (Saunders College Publishing, Fort Worth, 1976).

[8] Santhanam, P., Wind, S. & Prober, D. E. Localization, superconducting fluctuations, and superconductivity in thin films and narrow wires of aluminum. Physical Review B (1987).

[9] Pierre, F. & Birge, N. Dephasing by Extremely Dilute Magnetic Impurities Revealed by Aharonov-Bohm Oscillations. Physical Review Letters 89, 1–4 (2002).

[10] Albrecht, T. R., Grutter, P., Horne, D. & Rugar, D. Frequency modulation detection using high Q cantilevers for enhanced force microscope sensitivity. Journal of Applied Physics 668–673 (1991).

[11] Huang, N. E. et al. The empirical mode decomposition and the Hilbert spectrum for nonlinear and non-stationary time series analysis. Proceedings of the Royal Society A: Mathematical, Physical and Engineering Sciences 454, 903–995 (1998).

[12] Stuart, A. & Ord, J. K. Kendall's Advanced Theory of Statistics (Oxford University Press, New York, 1987), 5th edn.